Control of Three-Phase Bidirectional Current-Source Converter to Inject Balanced Three-Phase Currents Under Unbalanced Grid Voltage Condition

Vishal Vekhande, *Student Member, IEEE*, Kanakesh V. K., and Baylon G. Fernandes, *Member, IEEE*

***Abstract*—A single-stage, bidirectional, current-source converter (CSC) topology to interface a dc microgrid with an ac grid is reported in the literature. In this topology, under a balanced grid voltage condition, the dc-link inductor current can be regulated over a wide range—from zero to rated value—while the ac-side current has low harmonic distortion. However, unbalanced grid voltages result in second-harmonic pulsation in the current and power on the dc side of the converter. In addition, the ac-side currents will be unbalanced due to the presence of a negative-sequence component. This would result in undesired tripping of the converter if one of the phase currents exceeded its rated value. Various control loop structures for the operation of voltage-source converter under unbalanced grid voltage conditions are reported in the literature. However, use of similar control loop structures for CSC may lead to unstable operation. Therefore, a control scheme to inject balanced three-phase currents into the ac grid under an unbalanced grid voltage condition is proposed in this paper. The stability of the proposed control scheme is studied using a small-signal model of the converter. Performance of the proposed control scheme is studied using MATLAB/Simulink and is experimentally validated.**

***Index Terms*—Bidirectional, current-source converter (CSC), dc–ac, stability, unbalanced grid.**

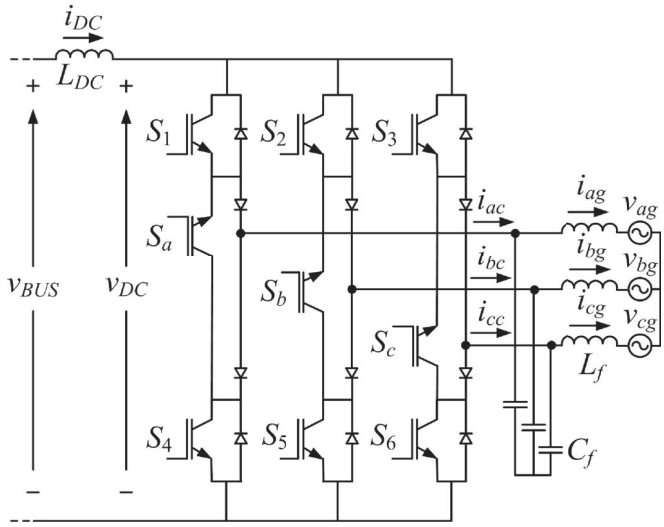

Fig. 1. Bidirectional CSC.

I. Introduction

THE voltage-source converter (VSC) is a converter topology that is commonly used to interface a dc microgrid with a utility ac grid that has a bidirectional power flow capability. However, reliability of this converter is low due to the presence of a large electrolytic capacitor across the dc-link [1]–[6]. Film capacitor-based VSC has lower energy density, higher cost, and/or employ additional active ripple reduction circuits [5], [6]. Further, VSC requires an additional dc–dc boost converter to interface a low-voltage dc microgrid with an ac grid [7], [8]. In contrast, a conventional current-source inverter (CSI) does not require any electrolytic capacitor for energy storage, and an additional dc–dc converter for dc-side voltage boosting. Therefore, CSI exhibits higher reliability and power density than the VSC + dc–dc boost converter topology, with comparable efficiency [8]–[11]. However, neither the dc-link inductor current of the CSI nor the dc microgrid bus voltage can be reversed. Therefore, this inverter has a unidirectional power flow capability. In [12], it is proposed to connect an additional dc–dc converter on the dc microgrid side to allow a reversal of the dc-link inductor current. These multiple conversion stages reduce the overall efficiency and reliability of the system.

A single-stage current-source converter (CSC) topology shown in Fig. 1 is proposed for battery charging/discharging, and dc motor drive application in [13]. In [14], the use of this converter topology as an interface between the dc microgrid and the utility ac grid is suggested. In this converter, power flow can be reversed from the ac grid to the dc microgrid by reversing the dc-link inductor current. Further, this dc-link inductor current can be regulated over a wide range—from zero to rated value—while the ac-side current has low harmonic distortion.

The presence of single-phase loads and unsymmetrical faults cause unbalance in grid voltages at the distribution level. These unbalanced grid voltages result in a second-harmonic pulsation in the power, voltage, and current on the dc side of the converter [15]–[22], [24]. This pulsation in the current results in a fundamental frequency negative-sequence and third-harmonic positive-sequence currents on the ac side [15], [18], [21], [26]. The converter current will be unbalanced due to the presence of this negative-sequence component. Under such condition, the converter would trip if one of the phase currents exceeded the rated value. This may cause system instability and cascaded failure of the power system if the generation or load on the dc side

Manuscript received March 8, 2015; revised June 18, 2015, September 1, 2015, and November 6, 2015; accepted November 11, 2015. Date of publication November 24, 2015; date of current version March 25, 2016. This work was supported in part by the Ministry of New and Renewable Energy, Government of India under the project "National Centre for Photovoltaic Research and Education." Recommended for publication by Associate Editor M. Molinas.

The authors are with the Department of Electrical Engineering, Indian Institute of Technology Bombay, Mumbai 400076, India (e-mail: vekhande@ee.iitb.ac.in; kanakeshvk@gmail.com; bgf@ee.iitb.ac.in).

Digital Object Identifier 10.1109/TPEL.2015.2503352

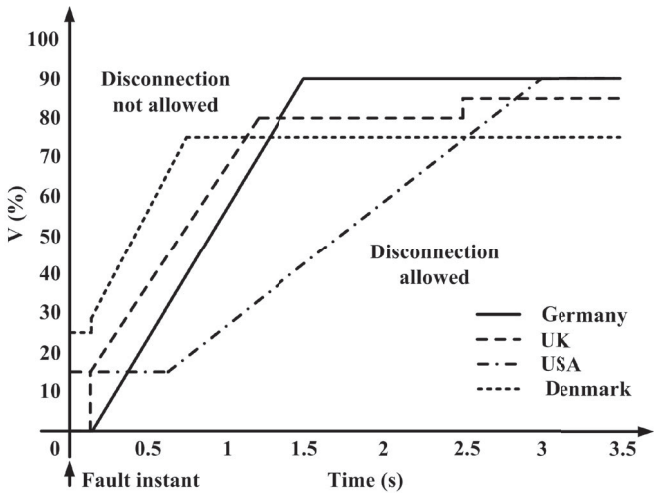

Fig. 2. Limiting voltage profile at the point of common coupling [28].

is significantly high [27]. Therefore, the recent grid codes have made it mandatory that the converter stays operational if the grid voltage is above the limits shown in Fig. 2 [24], [28], [29].

The operation of VSC under unbalanced grid voltage condition is well reported in the literature [16]–[24], [30], [31]. The control strategies reported in [16]–[20], [30], [31] are based on the dual-frame controller: one controller in the positive and the other in the negatively rotating synchronous reference frames. A controller based on the direct power control technique is reported in [21]–[23], wherein decomposition of positive- and negative-sequence components is not required. In these schemes, the control target is either to maintain the active power constant or balance the grid currents. In [24], it is proposed to inject zero sequence current into the grid, using a four-leg inverter. This offers increased control flexibility under unbalanced grid voltage condition. In all the above schemes, the undesired second harmonic pulsation in the control variables is eliminated using either a low-pass/notch filter, or suitably designing the proportional-integral (PI) regulator [16], [17], [32]. Moreover, the modulation index is calculated by dividing the dq-axis reference voltage magnitudes by actual dc-link voltage v_{DC} [17], [20]. In case of CSC, similar control loop structures may lead to unstable operation, as explained in this paper.

Although the low-voltage-ride-through capability of CSCs under balanced grid voltage sags is well discussed in the literature [27], [29], [33]–[37], the control of CSC under unbalanced grid voltage conditions has not received much attention from researchers [32]. Control of CSC with a *CL* filter at the output is a dual of VSC with an *LC* filter [38], [39]. However, CSC has lower phase margin as compared to VSC [39]. This margin further reduces due to the low-pass and notch filters, used to eliminate the second-harmonic pulsation in the control variables [16]. Therefore, stability of the control loop structure should be carefully examined when CSC is controlled using the similar control loop structures discussed above for VSC. In [15], it is proposed to generate unbalanced switching pattern under unbalanced grid voltage condition for a current-source rectifier (CSR) application. In [40], positive- and negative-sequence modulation indexes with appropriate phase angles are generated for a CSC interfacing a superconducting magnetic energy storage system with an unbalanced grid. In these schemes, the active power is maintained constant, which results in unbalanced grid currents. Two control strategies are proposed in [32] for a CSI that interfaces renewable energy sources to the grid. The first control strategy aims at injecting balanced three-phase currents to the grid, while either active or reactive powers are maintained constant in the second control strategy. The control loop structure to regulate the oscillatory dc-link current and its stability are not discussed in [32].

In this paper, a control strategy is proposed to inject balanced three-phase currents into the utility ac grid under unbalanced grid voltage conditions. However, injection of balanced ac currents into unbalanced grid voltages introduces a 100-Hz oscillation in an instantaneous active power. As a result, it is impossible to make the dc-link inductor current constant. Therefore, the dc-link inductor current is controlled around an average value. Further, it is proposed to eliminate the negative-sequence current component from the grid current by introducing a second-harmonic oscillation in the modulation index. The desired amplitude and phase of this oscillation are derived using PI regulators, such that the negative-sequence d- and q-axes current components observed in the negatively rotating synchronous reference frame are regulated to zero. Further, a small-signal model of the CSC is developed. The stability of the proposed control loop is studied using this model of the converter.

The key contributions of this paper are as follows.

1) A control strategy is proposed for CSC to inject balanced three-phase currents into the utility ac grid under unbalanced grid voltage conditions. Though a control strategy is proposed in [32] for a CSI to inject balanced three-phase currents into the unbalanced grid, the control loop structure to regulate the oscillatory dc-link current is not shown. Owing to the inherent lower phase margin of CSC compared to VSC [39], and the delays introduced by the filters in the control loop [16], the careful evaluation of the stability of this closed-loop controller is important. For the same reasons, it is not possible to control the CSC using the similar control loop structures that of VSC.
2) In the proposed control strategy, the negative-sequence current component is eliminated from the grid current.
3) The effectiveness of the proposed control scheme is tested based on the percentage unbalance in the grid currents, grid current total harmonic distortion (THD), peak-to-peak ripple in the dc-link current, current stress, and voltage stress on the devices at various unbalance levels in the grid voltages.
4) A small-signal model of the CSC is developed. It is useful to evaluate the stability of the conventional and the proposed control loops.

This paper is organized as follows: The operation of the three-phase bidirectional CSC topology is explained in Section II. A basic control strategy that does not provide any compensation during unbalanced grid voltage conditions is explained in Section III. In Section IV, the possible control loop structures are evaluated under unbalanced grid voltage conditions using a

TABLE I
CONVERTER SWITCHING STATES: INVERTER MODE OF OPERATION

Switching state	Switches	$i_{\rm ac}$	$i_{\rm bc}$	$i_{\rm cc}$
i_{1i}	S_1, S_6	$+i_{\rm DC}$	0	$-i_{\rm DC}$
i_{2i}	S_2, S_6	0	$+i_{\rm DC}$	$-i_{\rm DC}$
i_{3i}	S_2, S_4	$-i_{\rm DC}$	$+i_{\rm DC}$	0
i_{4i}	S_3, S_4	$-i_{\rm DC}$	0	$+i_{\rm DC}$
i_{5i}	S_3, S_5	0	$-i_{\rm DC}$	$+i_{\rm DC}$
i_{6i}	S_1, S_5	$+i_{\rm DC}$	$-i_{\rm DC}$	0
$i_{0\rm ai}$	S_1, S_4	0	0	0
$i_{0\rm bi}$	S_2, S_5	0	0	0
$i_{0\rm ci}$	S_3, S_6	0	0	0

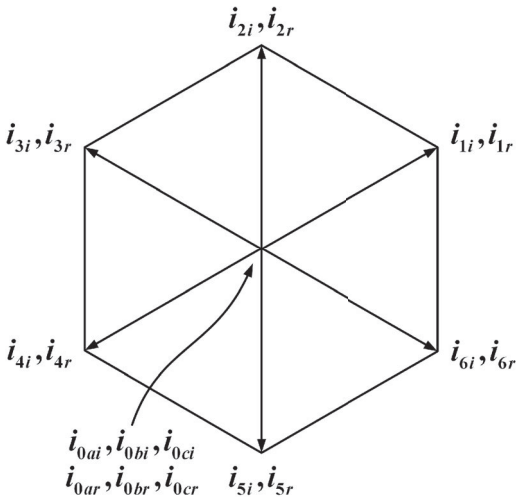

Fig. 3. CSI and 3SW-CSR space vectors.

small-signal model of the converter. The control scheme proposed for the injection of balanced three-phase grid currents is explained in Section V. The performance of the control schemes is studied using MATLAB/Simulink and is experimentally validated in Sections VI and VII, respectively. Finally, the conclusions of the paper are given in Section VIII.

II. THREE-PHASE BIDIRECTIONAL CSC

The three-phase bidirectional CSC topology is shown in Fig. 1. This converter is a combination of a three-phase CSI and a three-phase three-switch current-source rectifier (3SW-CSR) [13], [14], [41]. It has two broad modes of operation, namely, inverter and rectifier.

Inverter mode: Switches S_1–S_6 constitute the three-phase CSI. These switches provide the forward path for the dc-link inductor current $i_{\rm DC}$. Switches S_1, S_2, and S_3 are known as upper group switches, while S_4, S_5, and S_6 are known as the lower group switches. At any instant, one switch from the upper group and one switch from the lower group conduct in order to avoid the open circuit of the dc-link inductor $L_{\rm DC}$. Current $i_{\rm DC}$ is controlled using the current space vector modulation (SVM) technique [42]–[44]. There are nine valid switching states, as given in Table I. The space vector diagram is shown in Fig. 3. Switching states $i_{0\rm ai}$, $i_{0\rm bi}$, and $i_{0\rm ci}$ are shoot-through states, and switching states i_{1i}–i_{6i} are powering states.

TABLE II
CONVERTER SWITCHING STATES: RECTIFIER MODE OF OPERATION

Switching state	Switches	$i_{\rm ac}$	$i_{\rm bc}$	$i_{\rm cc}$
i_{1r}	S_c, S_a	$-i_{\rm DC}$	0	$+i_{\rm DC}$
i_{2r}	S_c, S_b	0	$-i_{\rm DC}$	$+i_{\rm DC}$
i_{3r}	S_a, S_b	$+i_{\rm DC}$	$-i_{\rm DC}$	0
i_{4r}	S_a, S_c	$+i_{\rm DC}$	0	$-i_{\rm DC}$
i_{5r}	S_b, S_c	0	$+i_{\rm DC}$	$-i_{\rm DC}$
i_{6r}	S_b, S_a	$-i_{\rm DC}$	$+i_{\rm DC}$	0
$i_{0\rm ar}$	S_a	0	0	0
$i_{0\rm br}$	S_b	0	0	0
$i_{0\rm cr}$	S_c	0	0	0

Rectifier mode: Switches S_a–S_c constitute the 3SW-CSR. These switches provide the reverse path for $i_{\rm DC}$. At any instant, at least one switch conducts. Current $i_{\rm DC}$ is controlled using the SVM technique [41], [45]. There are nine valid switching states, as given in Table II and shown in Fig. 3. The single switch conduction states $i_{0\rm ar}$, $i_{0\rm br}$, and $i_{0\rm cr}$ provide a freewheeling path for $i_{\rm DC}$. Switching states i_{1r}–i_{6r} are the powering states.

III. CONTROL STRATEGY

Fig. 4 shows the block diagram of the control strategy to regulate the dc-link inductor current. The phase angle information of the ac grid voltage is obtained using a three-phase phase-locked loop. Depending on the direction and magnitude of the desired active power flow, the dc-link current reference $i^*_{\rm DC}$ is generated by an external controller (not shown in the block diagram.) The error between $i^*_{\rm DC}$ and the sensed inductor current $i_{\rm DC}$ is processed by the PI regulator. The output of the PI regulator is the d-axis reference current i^*_d of the converter. The external controller also sets the q-axis reference current value i^*_q based on the desired reactive power flow. The current references i^*_d and i^*_q are then transformed from a synchronous to a stationary reference frame. Magnitude and angular position of the reference current space vector $|\vec{i}^*|$ and γ, respectively, are calculated using the stationary frame reference currents i^*_α and i^*_β. Further, the modulation index m is calculated by dividing the reference current space vector magnitude $|\vec{i}^*|$ by the actual dc-link current $i_{\rm DC}$, as shown in Fig. 4.

The modulation index m and the angular position γ are fed to the converter SVM block. This block computes the active time periods of the switching states and generates the gate signals. The inverter section is activated if the reference dc-link current $i^*_{\rm DC}$ is positive, and gate pulses for switches S_1–S_6 are generated. In this case, the gate pulses of switches S_a–S_c are disabled. The rectifier section, which generates gate pulses for switches S_a–S_c, is activated if $i^*_{\rm DC}$ is negative. In this case, gate pulses of switches S_1–S_6 are disabled. This eliminates the need for a multistep commutation process [46], [47].

Unlike that in VSC, in this converter, the maximum value of the reactive power that can be supplied depends on the amount of the active power exchanged with the grid [14], [48]. Further, the 3SW-CSR can have a maximum displacement angle of $\pm 30^\circ$ only [46], [49]. Owing to this restricted reactive power transfer capability, only a unity power factor operation is considered in further sections.

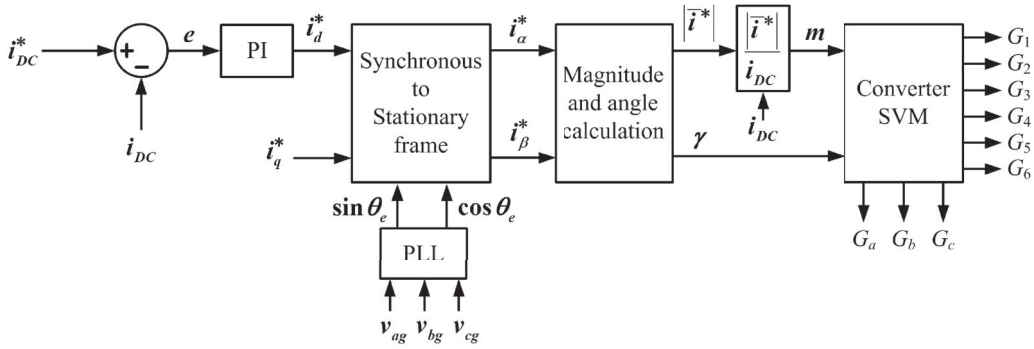

Fig. 4. Block diagram of the control scheme to regulate the dc-link inductor current.

IV. Control of the Converter Under Unbalanced Grid Voltage Conditions

In this section, possible control loop structures are evaluated under unbalanced grid voltage conditions. Detailed derivations of the small-signal models used in this section are given in Appendixes.

A. No Compensation During Unbalanced Grid Voltage Conditions

The control strategy presented in Section III does not provide any compensation during unbalanced grid voltage conditions. Therefore, the converter draws/injects pulsating active and reactive powers from/to the grid. The instantaneous active power p (reactive power q) can be represented as a summation of a constant value P_o (Q_o) and two orthogonal second-harmonic oscillating signals having peak values P_c and P_s (Q_c and Q_s) [16], [22]–[25] as

$$p = P_o + P_c\cos(2\omega t) + P_s\sin(2\omega t) \tag{1}$$

and

$$q = Q_o + Q_c\cos(2\omega t) + Q_s\sin(2\omega t) \tag{2}$$

In this case, although the average value of $i_{\rm DC}$ is the same as its reference value, it has a second-harmonic pulsation, proportional to the pulsation in the active power. Hence, it can also be represented as a summation of a constant value $I_{\rm DC}$ and two orthogonal second-harmonic oscillating signals having peak values $I_{\rm dcc}$ and $I_{\rm dcs}$ as

$$i_{\rm DC} = I_{\rm DC} + I_{\rm dcc}\cos(2\omega t) + I_{\rm dcs}\sin(2\omega t). \tag{3}$$

Fig. 5 shows the nature of various control loop signals under such operating condition. The presence of second-harmonic pulsation in e, i^*_d, and $|\bar{i}^*|$ can be observed. Therefore, $|\bar{i}^*|$ can also be represented as a summation of a constant value I^* and two orthogonal second-harmonic oscillating signals having peak values I^*_c and I^*_s as

$$|\bar{i}^*| = I^* + I^*_c\cos(2\omega t) + I^*_s\sin(2\omega t). \tag{4}$$

The equation for a grid current space vector can be written as

$$\bar{i}_g = m\, i_{\rm DC} e^{j(\omega t+\phi)} \tag{5}$$

where ϕ is the power factor angle and m is

$$m = \frac{|\bar{i}^*|}{i_{\rm DC}}. \tag{6}$$

Using (3), (4), and (6) in (5) gives

$$\bar{i}_g = \left[\frac{I^* + I^*_c\cos(2\omega t) + I^*_s\sin(2\omega t)}{I_{\rm DC} + I_{\rm dcc}\cos(2\omega t) + I_{\rm dcs}\sin(2\omega t)}\right] \times \left[I_{\rm DC} + I_{\rm dcc}\cos(2\omega t) + I_{\rm dcs}\sin(2\omega t)\right] e^{j(\omega t+\phi)}. \tag{7}$$

After simplification, the grid current space vector can be expressed as

$$\bar{i}_g = I^* e^{j(\omega t+\phi)} + \frac{I^*_c}{2}\left[e^{-j(\omega t-\phi)} + e^{j(3\omega t+\phi)}\right] - \frac{I^*_s}{2}\left[e^{-j(\omega t-\phi+\frac{\pi}{2})} + e^{j(3\omega t+\phi+\frac{\pi}{2})}\right]. \tag{8}$$

The following components are present in the above equation:

1) fundamental frequency positive sequence;
2) fundamental frequency negative sequence;
3) third-harmonic positive sequence.

The fundamental frequency negative-sequence component causes unbalance in the grid currents. The third-harmonic positive sequence component contributes to increase in the THD..

In addition, the stability of the control scheme shown in Fig. 5 is studied using the small-signal model of the converter. The detailed analysis is given in Appendix A. Fig. 6(a) and (b) shows the root loci of the closed-loop transfer function of the controller for the inverter and rectifier modes of operation, respectively. It can be observed that this control scheme is stable when the proportional gain $K_P > 0.6$, and $K_P > 0$, for the inverter and rectifier modes of operation, respectively.

B. Modified Control Scheme to Inject Balanced Three-Phase Grid Currents

It can be concluded from the above discussion that the uncontrolled second-harmonic oscillation in the reference current space vector $|\bar{i}^*|$ leads to a fundamental frequency negative-sequence and third-harmonic positive-sequence components in the grid currents. This second-harmonic oscillation in $|\bar{i}^*|$ is due to the oscillations in various control loop signals that are caused by the oscillating dc-link current $i_{\rm DC}$. These oscillations in the control loop signals can be eliminated by filtering the $i_{\rm DC}$

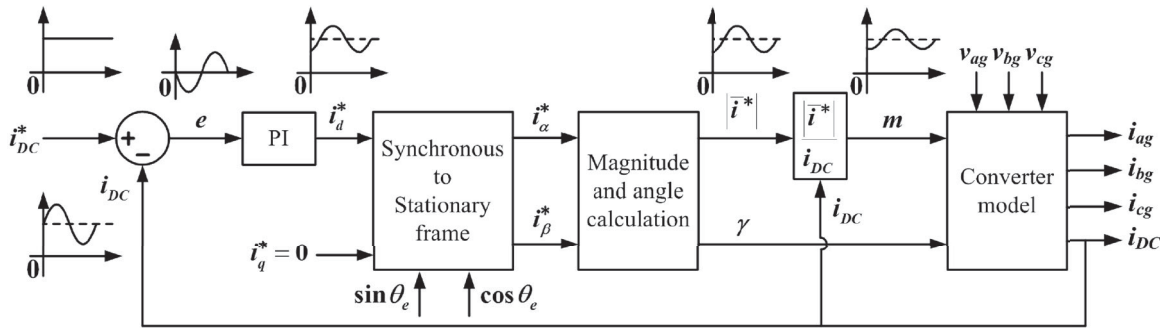

Fig. 5. Nature of various control loop signals under an unbalanced grid voltage condition.

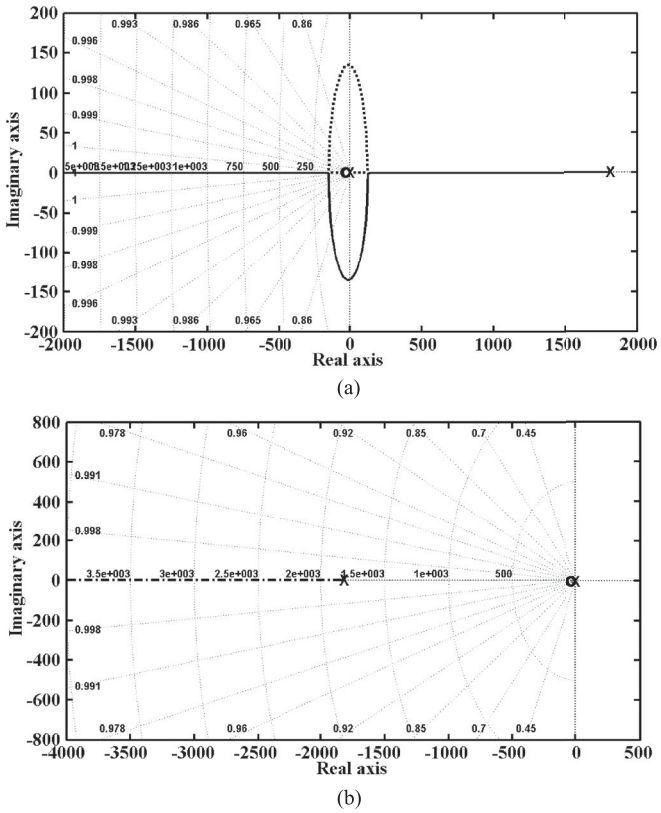

Fig. 6. Root loci of the closed-loop transfer function of the controller for the control scheme without unbalanced grid voltage compensation for (a) inverter and (b) rectifier modes of operation.

signal using a 100-Hz notch filter, as shown in Fig. 7. With this modification, (4) changes to

$$|\bar{i}^*| = I^*. \tag{9}$$

Using (3), (6), and (9) in (5) gives

$$\bar{i}_g = \left[\frac{I^*}{I_{\rm DC} + I_{\rm dcc}\cos(2\omega t) + I_{\rm dcs}\sin(2\omega t)}\right] \times \left[I_{\rm DC} + I_{\rm dcc}\cos(2\omega t) + I_{\rm dcs}\sin(2\omega t)\right] e^{j(\omega t+\phi)}. \tag{10}$$

Further simplification gives

$$\bar{i}_g = I^* e^{j(\omega t+\phi)}. \tag{11}$$

It can be concluded from the above equation that the grid currents are perfectly balanced and free from harmonic components.

Further, the stability of the modified control scheme shown in Fig. 7 is studied using the small-signal model of the converter. The detailed analysis is given in Appendix B. Fig. 8(a) and (b) shows the root loci of the closed-loop transfer function of the controller for the inverter and rectifier modes of operation, respectively. During the inverter mode of operation, at least one pole exists on the right-hand side of the imaginary axis for any finite value of K_P. Therefore, the modified control scheme is unstable in the inverter mode of operation, while it is stable for the rectifier mode of operation.

From the discussions in Sections IV-A and IV-B, the following points can be noted.

1) The control scheme without unbalance compensation results in unbalanced grid currents under unbalanced grid voltage conditions. The operation is stable during inverter and rectifier modes of operation.
2) The modified control scheme produces balanced currents under unbalanced grid voltage conditions. However, it is unstable in the inverter mode of operation.
3) In both the control schemes, the output of the PI regulator is the reference d-axis current i_d^*. The modulation index m is calculated by dividing the reference current space vector magnitude $|\bar{i}^*|$ by the actual dc-link current $i_{\rm DC}$. The difference between these two control schemes is the presence of a 100-Hz notch filter in the feedback loop in the case of the modified control scheme.
4) Therefore, it can be concluded that the operation becomes unstable because of the notch filter when the $(\frac{1}{i_{\rm DC}})$ term is used to generate the modulation index.

This limitation is addressed in the following control scheme.

V. Proposed Control Scheme to Inject Balanced Three-Phase Grid Currents

In the control schemes explained in previous sections, the output of the PI regulator is the reference d-axis current i_d^*. Instead, if it is the reference modulation index, then the $(\frac{1}{i_{\rm DC}})$ term in the control loop can be avoided. The resulting block diagram is shown in Fig. 9. The error between $i_{\rm DC}^*$ and the filtered dc-link current $I_{\rm DC}$ is processed by the PI regulator PI_1. The output of PI_1 is the d-axis modulation index m_d^*.

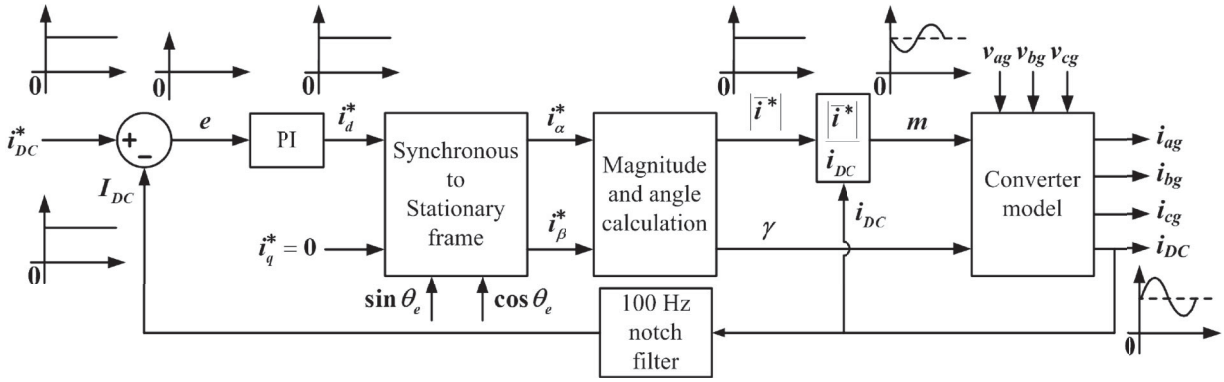

Fig. 7. Block diagram of the modified control scheme to inject balanced three-phase grid currents under unbalanced grid voltage conditions.

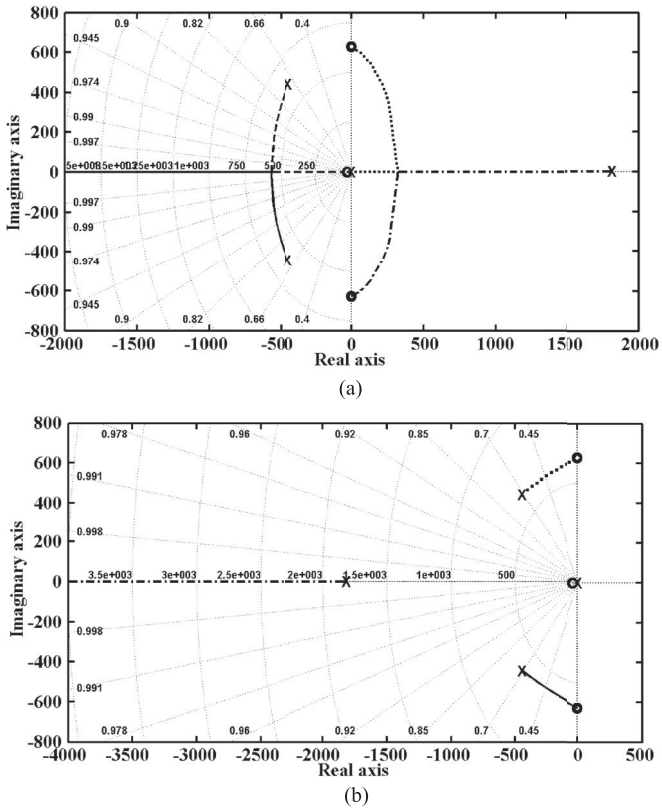

Fig. 8. Root loci of the closed-loop transfer function of the controller for the modified control scheme to inject balanced three-phase grid currents for (a) inverter and (b) rectifier modes of operation.

The q-axis modulation index m^*_q is set to zero to achieve the unity power factor operation. The modulation index M and the angular position of the modulation signal γ are calculated using the stationary frame modulation indexes m^*_α and m^*_β. In the proposed scheme, although the current $i_{\rm DC}$ has a second-harmonic pulsation under unbalanced grid voltage conditions, the control loop signals e, m^*_d, and M are constant due to the presence of a 100-Hz notch filter in the feedback loop. However, the modulation index m should pulsate to produce balanced three-phase currents. The mathematical expression for such a pulsating m is developed in Section V-A.

A. *Mathematical Expression for the Modulation Index* m

In (10), the first term represents the modulation index m. Therefore

$$m = \frac{I^*}{I_{\rm DC} + I_{\rm dcc}\cos(2\omega t) + I_{\rm dcs}\sin(2\omega t)}. \tag{12}$$

In the modified control scheme, the instantaneous value of m is calculated by solving the equation above by using instantaneous numerical values of its numerator and denominator terms. However, it is also possible to find the mathematical expression for m. It is derived as follows.

Using the power series theorem, (12) can be written as

$$\begin{aligned} m = \; I^*\Bigg\{ & \frac{1}{I_{\rm DC}} - \frac{[I_{\rm dcc}\cos(2\omega t) + I_{\rm dcs}\sin(2\omega t)]}{I^2_{\rm DC}} \\ & + \frac{[I_{\rm dcc}\cos(2\omega t) + I_{\rm dcs}\sin(2\omega t)]^2}{I^3_{\rm DC}} \\ & - \frac{[I_{\rm dcc}\cos(2\omega t) + I_{\rm dcs}\sin(2\omega t)]^3}{I^4_{\rm DC}} + \cdots \Bigg\}. \end{aligned} \tag{13}$$

After rearranging the terms, m can be expressed as

$$\begin{aligned} m = \; & M + M_c\cos(2\omega t) + M_s\sin(2\omega t) \\ & + M_{c4}\cos(4\omega t) + M_{s4}\sin(4\omega t) + \cdots \end{aligned} \tag{14}$$

where

$$\begin{aligned} M &= I^*\left[\frac{1}{I_{\rm DC}} + \frac{I^2_{\rm dcc}}{2\,I^3_{\rm DC}} + \frac{I^2_{\rm dcs}}{2\,I^3_{\rm DC}}\right] \\ M_c &= I^*\left[-\frac{I_{\rm dcc}}{I^2_{\rm DC}} - \frac{3}{4}\frac{I^3_{\rm dcc}}{I^4_{\rm DC}} - \frac{3}{4}\frac{I_{\rm dcc}I^2_{\rm dcs}}{I^4_{\rm DC}} + \cdots\right] \\ M_s &= I^*\left[-\frac{I_{\rm dcs}}{I^2_{\rm DC}} - \frac{3}{4}\frac{I^3_{\rm dcs}}{I^4_{\rm DC}} - \frac{3}{4}\frac{I^2_{\rm dcc}\,I_{\rm dcs}}{I^4_{\rm DC}} + \ldots\right] \\ M_{c4} &= I^*\left[\frac{I^2_{\rm dcc}}{2\,I^3_{\rm DC}} - \frac{I^2_{\rm dcs}}{2\,I^3_{\rm DC}} + \ldots\right] \\ M_{s4} &= I^*\left[\frac{I_{\rm dcc}I_{\rm dcs}}{I^3_{\rm DC}} + \ldots\right]. \end{aligned}$$

The complete derivation process is given in Appendix D.

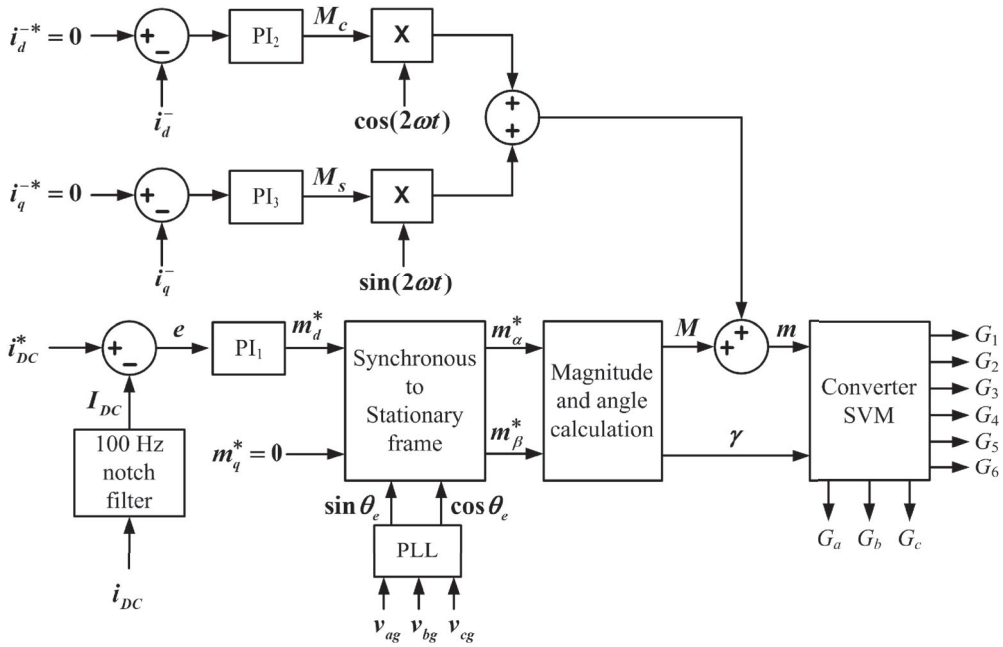

Fig. 9. Block diagram of the proposed control scheme to inject balanced three-phase grid currents under unbalanced grid voltage conditions.

From (14), it can be concluded that the modulation index m should have higher order harmonic terms in addition to a constant value M, to compensate for the second-order oscillation in $i_{\rm DC}$. Such a modulation index will produce balanced grid currents. The coefficients M_{c4} and M_{s4} are very small, because their expression contains the product of two ac terms in the numerator and the third power term of the average dc-link current in the denominator. Therefore, neglecting these terms, the expression for the modulation index m can be written as

$$m = M + M_c\cos(2\omega t) + M_s\sin(2\omega t). \tag{15}$$

The negative-sequence components can be eliminated from the grid currents if the modulation index follows the pattern represented by (15). In this equation, the value of M is determined using the control loop structure explained earlier, and shown in Fig. 9. The necessary condition for M_c and M_s to eliminate the negative-sequence components is derived in Section V-B.

B. Necessary Condition for M_c and M_s to Eliminate the Negative Sequence Components From Grid Currents

Using (3), (6), and (15) in (5) gives

$$\begin{aligned}\bar{i}_g = {} & [M + M_c\cos(2\omega t) + M_s\sin(2\omega t)] \\ & \times[I_{\rm DC} + I_{\rm dcc}\cos(2\omega t) + I_{\rm dcs}\sin(2\omega t)]e^{j(\omega t+\phi)}.\end{aligned} \tag{16}$$

After simplification and rearranging the terms, the expression for the grid current space vector can be written as

$$\begin{aligned}\bar{i}_g = {} & \left[MI_{\rm DC} + \frac{M_cI_{\rm dcc}}{2} + \frac{M_sI_{\rm dcs}}{2}\right]e^{j(\omega t+\phi)} \\ & + \left[\frac{MI_{\rm dcc}}{2} + \frac{M_cI_{\rm DC}}{2}\right]e^{-j(\omega t-\phi)} \\ & - \left[\frac{MI_{\rm dcs}}{2} + \frac{M_sI_{\rm DC}}{2}\right]e^{-j(\omega t-\phi+\frac{\pi}{2})} \\ & + \left[\frac{MI_{\rm dcc}}{2} + \frac{M_cI_{\rm DC}}{2}\right]e^{j(3\omega t+\phi)} \\ & - \left[\frac{MI_{\rm dcs}}{2} + \frac{M_sI_{\rm DC}}{2}\right]e^{j(3\omega t+\phi+\frac{\pi}{2})} \\ & + \frac{M_cI_{\rm dcc}}{4}\left[e^{-j(3\omega t-\phi)} + e^{j(5\omega t+\phi)}\right] \\ & - \frac{M_cI_{\rm dcs}}{4}\left[e^{-j(3\omega t-\phi+\frac{\pi}{2})} + e^{j(5\omega t+\phi+\frac{\pi}{2})}\right] \\ & - \frac{M_sI_{\rm dcs}}{4}\left[e^{-j(3\omega t-\phi)} + e^{j(5\omega t+\phi)}\right] \\ & - \frac{M_sI_{\rm dcs}}{4}\left[e^{-j(3\omega t-\phi+\frac{\pi}{2})} + e^{j(5\omega t+\phi+\frac{\pi}{2})}\right].\end{aligned} \tag{17}$$

The complete derivation process is given in Appendix E. The following components are present in the above equation:

1) fundamental frequency positive sequence;
2) fundamental frequency negative sequence;
3) third-harmonic positive sequence;
4) third-harmonic negative sequence;
5) fifth-harmonic positive sequence.

The fundamental frequency negative-sequence components can be eliminated from the grid currents if

$$M_c = -\frac{MI_{\rm dcc}}{I_{\rm DC}} \quad \text{and} \quad M_s = -\frac{MI_{\rm dcs}}{I_{\rm DC}}. \tag{18}$$

Using (18) in (17) gives

$$\bar{i}_g = \left[MI_{\rm DC} - \frac{MI_{\rm dcc}^2}{2\,I_{\rm DC}} - \frac{MI_{\rm dcs}^2}{2\,I_{\rm DC}}\right]e^{j(\omega t+\phi)}$$

$$
\begin{aligned}
&- \frac{MI_{\rm dcc}^2}{4\,I_{\rm DC}}\left[e^{-j(3\omega t-\phi)} + e^{j(5\omega t+\phi)}\right] \\
&+ \frac{MI_{\rm dcc}I_{\rm dcs}}{4\,I_{\rm DC}}\left[e^{-j(3\omega t-\phi+\frac{\pi}{2})} + e^{j(5\omega t+\phi+\frac{\pi}{2})}\right] \\
&+ \frac{MI_{\rm dcs}^2}{4\,I_{\rm DC}}\left[e^{-j(3\omega t-\phi)} + e^{j(5\omega t+\phi)}\right] \\
&+ \frac{MI_{\rm dcs}I_{\rm dcc}}{4\,I_{\rm DC}}\left[e^{-j(3\omega t-\phi+\frac{\pi}{2})} + e^{j(5\omega t+\phi+\frac{\pi}{2})}\right]. \quad (19)
\end{aligned}
$$

Interestingly, by comparing (17) and (19), it can be noted that in addition to the fundamental frequency negative-sequence components, the third-harmonic positive-sequence components also get eliminated from the grid currents when M_c and M_s satisfy the conditions given in (18). However, a small percentage of the third-harmonic negative-sequence and fifth-harmonic positive-sequence components would be present in the grid currents.

C. Closed-Loop Control of Negative Sequence Currents

The required values of M_c and M_s to eliminate the negative-sequence components from the grid currents can be calculated using (18). It is also possible to generate these values using closed-loop controllers that regulate the dq-axes fundamental frequency negative-sequence currents i_d^- and i_q^- to zero. For this, it is necessary to find the correlation between the quantities M_c, M_s, i_d^-, and i_q^-. It is derived as follows.

Equation (17) represents the grid currents in the stationary reference frame. The expression for the grid current space vector in the negatively rotating synchronous reference frame can be written, by multiplying (17) with $e^{j(\omega t)}$, as

$$
\begin{aligned}
\bar{i}_g|_n = &\left[MI_{\rm DC} + \frac{M_cI_{\rm dcc}}{2} + \frac{M_sI_{\rm dcs}}{2}\right]e^{j(2\omega t+\phi)} \\
&+ \left[\frac{MI_{\rm dcc}}{2} + \frac{M_cI_{\rm DC}}{2}\right]e^{j(\phi)} \\
&- \left[\frac{MI_{\rm dcs}}{2} + \frac{M_sI_{\rm DC}}{2}\right]e^{j(\phi-\frac{\pi}{2})} \\
&+ \left[\frac{MI_{\rm dcc}}{2} + \frac{M_cI_{\rm DC}}{2}\right]e^{j(4\omega t+\phi)} \\
&- \left[\frac{MI_{\rm dcs}}{2} + \frac{M_sI_{\rm DC}}{2}\right]e^{j(4\omega t+\phi+\frac{\pi}{2})} \\
&+ \frac{M_cI_{\rm dcc}}{4}\left[e^{-j(4\omega t-\phi)} + e^{j(6\omega t+\phi)}\right] \\
&- \frac{M_cI_{\rm dcs}}{4}\left[e^{-j(4\omega t-\phi+\frac{\pi}{2})} + e^{j(6\omega t+\phi+\frac{\pi}{2})}\right] \\
&- \frac{M_sI_{\rm dcs}}{4}\left[e^{-j(4\omega t-\phi)} + e^{j(6\omega t+\phi)}\right] \\
&- \frac{M_sI_{\rm dcc}}{4}\left[e^{-j(4\omega t-\phi+\frac{\pi}{2})} + e^{j(6\omega t+\phi+\frac{\pi}{2})}\right]. \quad (20)
\end{aligned}
$$

In the above equation, the second and the third terms correspond to the dq-axes fundamental frequency negative-sequence currents. Therefore, these negative-sequence currents can be expressed as

$$
\begin{aligned}
i_d^- = &\left[\frac{MI_{\rm dcc}}{2} + \frac{M_cI_{\rm DC}}{2}\right]\cos\phi \\
&- \left[\frac{MI_{\rm dcs}}{2} + \frac{M_sI_{\rm DC}}{2}\right]\cos\left(\phi - \frac{\pi}{2}\right) \quad (21)
\end{aligned}
$$

and

$$
\begin{aligned}
i_q^- = &\left[\frac{MI_{\rm dcc}}{2} + \frac{M_cI_{\rm DC}}{2}\right]\sin\phi \\
&- \left[\frac{MI_{\rm dcs}}{2} + \frac{M_sI_{\rm DC}}{2}\right]\sin\left(\phi - \frac{\pi}{2}\right). \quad (22)
\end{aligned}
$$

In the above two equations, it can be observed that at unity power factor operation, the term M_c influences the magnitude of i_d^-, and the term M_s affects the magnitude of i_q^- only. Therefore, the second-harmonic oscillation required in order to obtain balanced grid currents can be introduced in the modulation index m using two orthogonal signals $[M_c\cos(2\omega t)]$ and $[M_s\sin(2\omega t)]$, as shown in Fig. 9. The value of the amplitude M_c is obtained using the PI regulator PI_2 that regulates the d-axis negative-sequence current i_d^- to zero. Similarly, amplitude M_s is generated by PI_3 that regulates i_q^- to zero.

The stability of the proposed control scheme is studied using the small-signal model of the converter. A detailed analysis is given in Appendix C. Identical closed-loop transfer functions are obtained for the inverter and rectifier modes of operation. The root locus of the closed-loop transfer function of the controller for the inverter and rectifier modes of operation is shown in Fig. 10. It can be observed that this control scheme has stable operation for the condition $0 < K_P < \infty$.

Further, stability of the control loops used to regulate the negative-sequence currents i_d^- and i_q^- is also studied. A detailed analysis is given in Appendix F. Both the controllers have identical root loci as shown in Fig. 11. It can be observed that these controllers have stable operation for the condition $0 < K_P < 0.1$.

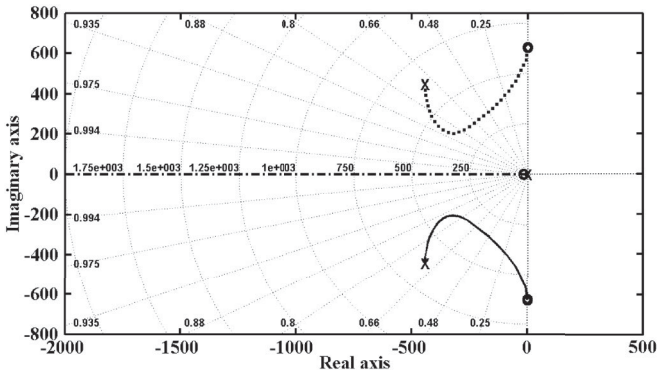

Fig. 10. Root locus of the closed-loop transfer function of the controller using the proposed control scheme to inject balanced three-phase grid currents for inverter and rectifier modes.

VI. Simulation Results

A 10-kVA converter interfacing a 415-V, 50-Hz, three-phase ac grid with a 300-V dc microgrid is simulated using

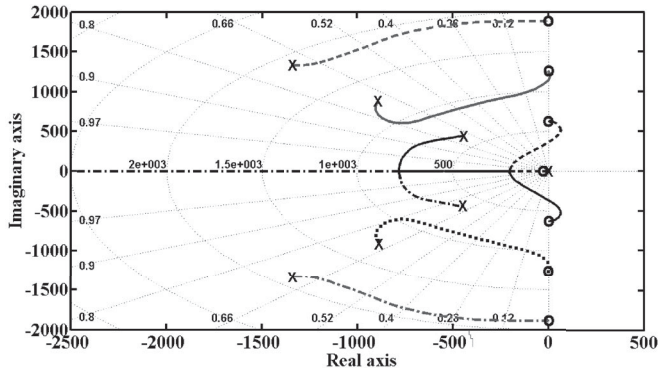

Fig. 11. Root locus of the closed-loop transfer function of the controller used to regulate the negative-sequence currents i_d^- and i_q^-.

TABLE III
SIMULATION PARAMETERS

Rated power	10 kVA
DC microgrid voltage, $v_{\rm BUS}$	300 V
Grid line voltage, V_g	415 V
DC inductor, $L_{\rm DC}$	5 mH
Filter inductor, L_f	3 mH
Filter capacitor, C_f	30 μF
Switching frequency	15 kHz

MATLAB/Simulink. The simulation parameters are given in Table III. Here, the dc microgrid bus voltage $v_{\rm BUS}$ is emulated using a dc source.

A. No Compensation During Unbalanced Grid Voltage Conditions

The performance of the control strategy presented in Section III and shown in Fig. 4 is studied under the balanced grid voltage condition, first. The current reference i_q^* is set equal to zero. Fig. 12(a) and (b) shows the variation of $i_{\rm DC}$ for the ramp changes in its reference value, in inverter and rectifier modes of operation, respectively. For these modes of operation, the grid phase voltage and current are shown in Fig. 12(c) and (d). It can be seen that the system is capable of operating at a high power factor in both the modes.

However, this control strategy can regulate the dc-link current only. Under an unbalanced grid voltage condition, though the average value of the dc-link current is maintained, it has a second-harmonic oscillation as seen in Fig. 13(b) and (c). If the modulation index is generated using the control block diagram that is shown in Fig. 4, the grid currents will be unbalanced, as seen in Fig. 13(d) and (e). The grid currents have a negative-sequence component. In addition, a third-harmonic component is also present, as observed in Fig. 13(f) and (g).

B. Proposed Control Scheme to Inject Balanced Three-Phase Grid Currents

The performance of the proposed control scheme, explained in Section V, is tested for 15% unbalance in grid voltages. It can be seen from Fig. 14(b) and (c) that the dc-link current has second-harmonic pulsation. In spite of this pulsation, balanced three-phase grid currents are obtained. This can be observed in Fig. 14(d) and (e). Fig. 14(f) and (g) shows the harmonic spectrum of phase-a grid current $i_{\rm ag}$ for the inverter and rectifier modes of operation, respectively. It can be seen that the percentage magnitude of the third-harmonic component has reduced significantly compared to that in Fig. 13(f) and (g). However, a small percentage of third- and fifth-harmonic components are present. These observations are in accordance with (19).

The recent grid codes have made it mandatory that the converter stays operational for few cycles, even though one of the phase voltages has reduced to 0%, as shown in Fig. 2 [28]. This corresponds to 100% unbalance in the grid voltages. The effectiveness of the proposed control scheme is also tested at various unbalance levels in the grid voltages. The percentage unbalance in grid voltages and currents are calculated using [50]

$$\%\ \text{unbalance} = \frac{\begin{array}{c}\text{max voltage (or current)}\\ \text{deviation from the average}\\ \text{phase voltage (or current)}\end{array}}{\begin{array}{c}\text{average phase voltage}\\ \text{(or current)}\end{array}}.100. \quad (23)$$

The percentage unbalance in three-phase grid currents is plotted against the percentage unbalance in three-phase grid voltages in Fig. 15(a) and (b) for the inverter and rectifier modes, respectively. It can be observed that there is a significant reduction in percentage unbalance in grid currents when the proposed control scheme is activated. Further, THD of the grid currents also improves, as observed in Fig. 15(c) and (d). This is due to the reduction in the third-harmonic component. It is interesting to note that although the dc-link current has a second-harmonic pulsation, its peak-to-peak amplitude reduces when the proposed control scheme is used. As a result, the current stress on the devices reduces approximately by 12% and 18%, as observed in Fig. 15(g) and (h), for inverter and rectifier modes of operation, respectively. This feature can also be observed by comparing Fig. 13(b) and (c) with Fig. 14(b) and (c). The voltage stress on the devices reduces monotonically as the percentage unbalance in the grid voltages increases, when no compensation is provided. On the other hand, this stress on the devices remains almost constant (approximately 3% variation) as observed in Fig. 15(i) and (j), when the proposed control scheme is used.

VII. EXPERIMENTAL RESULTS

In order to validate the simulation results, a laboratory prototype of the bidirectional current-fed converter is designed and fabricated. The parameters of the experimental setup are given in Table IV. Unbalance in the grid voltages is set at 15%. Here, the dc microgrid bus voltage $v_{\rm BUS}$ is emulated using a dc source, while the desired unbalance in the grid voltages is set by reducing the phase-a voltage using an autotransformer.

Fig. 16 shows the experimental results for the inverter mode of operation. It can be seen from Fig. 16(a) that the grid currents are unbalanced if there is no compensation during the unbalanced grid voltage condition. The resultant unbalance in the grid currents is 7%. The grid currents have a significant percentage of third- and fifth-harmonic currents. Therefore, its THD is higher,

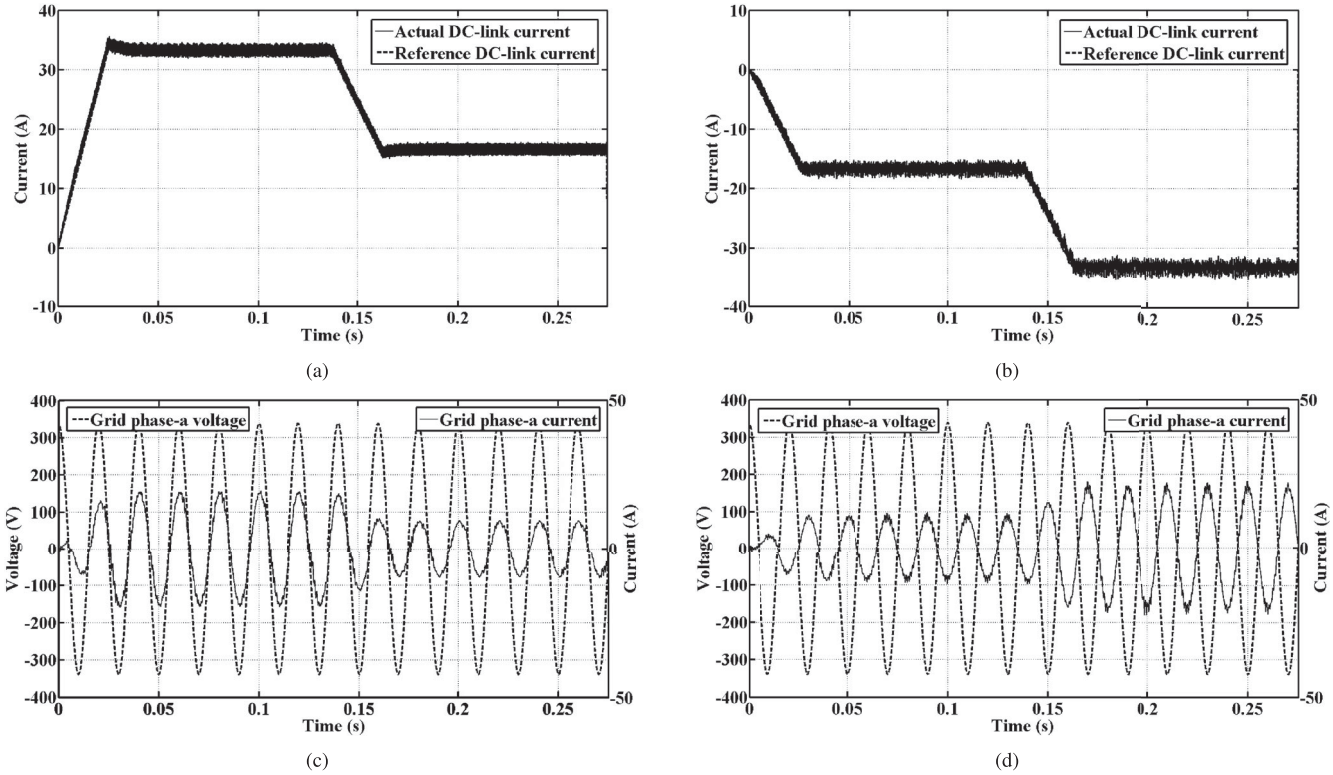

Fig. 12. Simulation results: Actual and reference dc-link currents for (a) inverter (b) rectifier modes of operation; grid phase voltage and current for (c) inverter (d) rectifier modes of operation under a balanced grid voltage condition.

TABLE IV
EXPERIMENTAL SETUP PARAMETERS

Rated power	1 kVA
DC microgrid voltage, v_{BUS}	105 V
Grid line voltage, V_g	125 V
DC inductor, L_{DC}	5 mH
Filter inductor, L_f	3 mH
Filter capacitor, C_f	30 μF
Switching frequency	4.5 kHz

as seen in Fig. 16(c). Balanced grid currents are obtained using the proposed control scheme, as observed in Fig. 16(b). In this case, unbalance in the grid currents is less than 1%. It can be seen in Fig. 16(d) that there is a significant reduction in the third-harmonic current component when the proposed control scheme is activated.

Similar results are obtained for the rectifier mode of operation, and they are shown in Fig. 17. The unbalance in the grid currents is 6%, and the THD is poor, as observed in Fig. 17(a) and (c), respectively, when no compensation is provided. The grid current unbalance reduces to 2% when the proposed control scheme is activated, as seen in Fig. 17(b). Further, the current THD improves due to the reduction in third-harmonic current component, as observed in Fig. 17(d).

VIII. CONCLUSION

A three-phase bidirectional converter based on a current source topology to interface a dc microgrid with the main ac grid is suggested. Under unbalanced grid voltage conditions, the dc-link current has a second-harmonic pulsation. In addition, the ac-side currents are unbalanced due to the presence of a negative-sequence component. This might result in undesired tripping of the converter. Balanced three-phase currents can be injected into the unbalanced grid voltages using a modified control scheme. However, it is found that the modified control scheme becomes unstable in the inverter mode of operation because of the notch filter and the $(\frac{1}{i_{\mathrm{DC}}})$ term that is used to generate the modulation index. Therefore, a control scheme is proposed, where the $(\frac{1}{i_{\mathrm{DC}}})$ term in the control loop is avoided. The stability of the proposed control scheme is analyzed using a small-signal model of the converter. The performance of the proposed control scheme is studied using MATLAB/Simulink and is experimentally validated.

APPENDIX A
STABILITY ANALYSIS OF THE CLOSED-LOOP CONTROLLER USING THE CONTROL SCHEME WITHOUT UNBALANCE COMPENSATION

From Fig. 1, the differential equation for dc-side of the converter can be written as

$$v_{\mathrm{BUS}} - L_{\mathrm{DC}}\frac{di_{\mathrm{DC}}}{dt} - v_{\mathrm{DC}} = 0. \tag{24}$$

The averaged equation can be written as

$$\langle v_{\mathrm{BUS}}(t)\rangle_{Ts} - L_{\mathrm{DC}}\frac{d\langle i_{\mathrm{DC}}(t)\rangle_{Ts}}{dt} - \langle v_{\mathrm{DC}}(t)\rangle_{Ts} = 0. \tag{25}$$

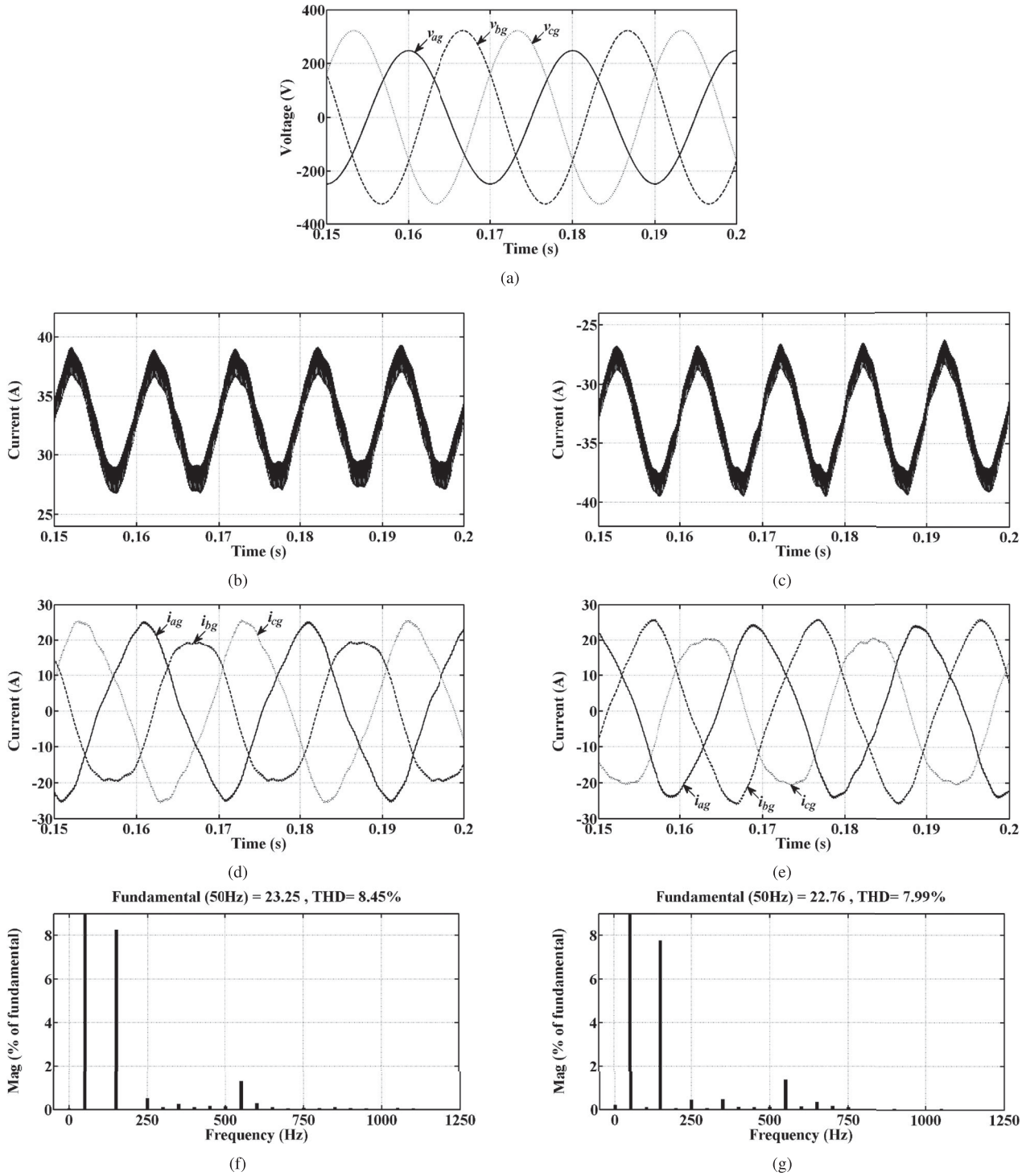

Fig. 13. Simulation results: (a) Unbalanced three-phase grid voltages; dc-link current for (b) inverter and (c) rectifier modes of operation; three-phase grid currents for (d) inverter and (e) rectifier modes of operation; harmonic spectrum of i_{ag} for (f) inverter and (g) rectifier modes of operation.

The power balance equation between converter dc and ac sides can be written as

$$\langle v_{\mathrm{DC}}(t)\rangle_{Ts}\langle i_{\mathrm{DC}}(t)\rangle_{Ts} = \frac{3}{2}\langle v_d(t)\rangle_{Ts}\langle i_d(t)\rangle_{Ts} + \frac{3}{2}\langle v_q(t)\rangle_{Ts}\langle i_q(t)\rangle_{Ts}. \quad (26)$$

Therefore

$$\langle v_{\mathrm{DC}}(t)\rangle_{Ts} = \frac{3}{2}\langle v_d(t)\rangle_{Ts}\frac{\langle i_d(t)\rangle_{Ts}}{\langle i_{\mathrm{DC}}(t)\rangle_{Ts}} + \frac{3}{2}\langle v_q(t)\rangle_{Ts}\frac{\langle i_q(t)\rangle_{Ts}}{\langle i_{\mathrm{DC}}(t)\rangle_{Ts}}. \quad (27)$$

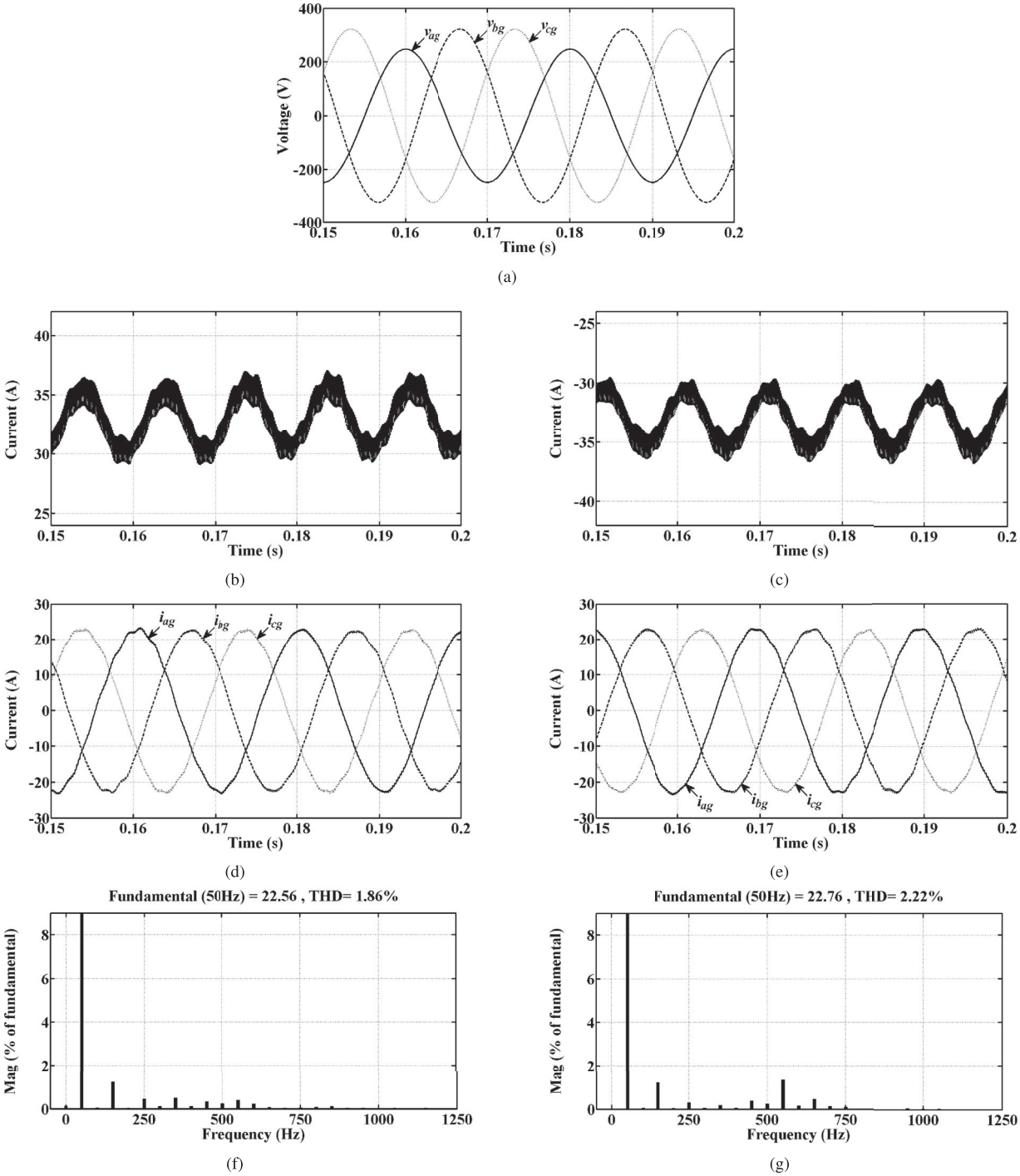

Fig. 14. Simulation results for the proposed control scheme. (a) Unbalanced three-phase grid voltages; dc-link current for (b) inverter and (c) rectifier modes of operation; three-phase grid currents for (d) inverter and (e) rectifier modes of operation; harmonic spectrum of i_{ag} for (f) inverter and (g) rectifier modes of operation.

Using (27) in (25) gives

$$\langle v_{\mathrm{BUS}}(t)\rangle_{Ts} - L_{\mathrm{DC}}\frac{d\langle i_{\mathrm{DC}}(t)\rangle_{Ts}}{dt} - \frac{3}{2}\langle v_d(t)\rangle_{Ts}\frac{\langle i_d(t)\rangle_{Ts}}{\langle i_{\mathrm{DC}}(t)\rangle_{Ts}} - \frac{3}{2}\langle v_q(t)\rangle_{Ts}\frac{\langle i_q(t)\rangle_{Ts}}{\langle i_{\mathrm{DC}}(t)\rangle_{Ts}} = 0. \tag{28}$$

After applying small perturbation, (28) becomes

$$V_{\mathrm{BUS}} + \widehat{v}_{\mathrm{BUS}}(t) - L_{\mathrm{DC}}\frac{dI_{\mathrm{DC}}}{dt} - L_{\mathrm{DC}}\frac{d\widehat{i}_{\mathrm{DC}}(t)}{dt} - \frac{3}{2}[V_d + \widehat{v}_d(t)]\left[\frac{I_d + \widehat{i}_d(t)}{I_{\mathrm{DC}} + \widehat{i}_{\mathrm{DC}}(t)}\right] - \frac{3}{2}[V_q + \widehat{v}_q(t)]\left[\frac{I_q + \widehat{i}_q(t)}{I_{\mathrm{DC}} + \widehat{i}_{\mathrm{DC}}(t)}\right] = 0. \tag{29}$$

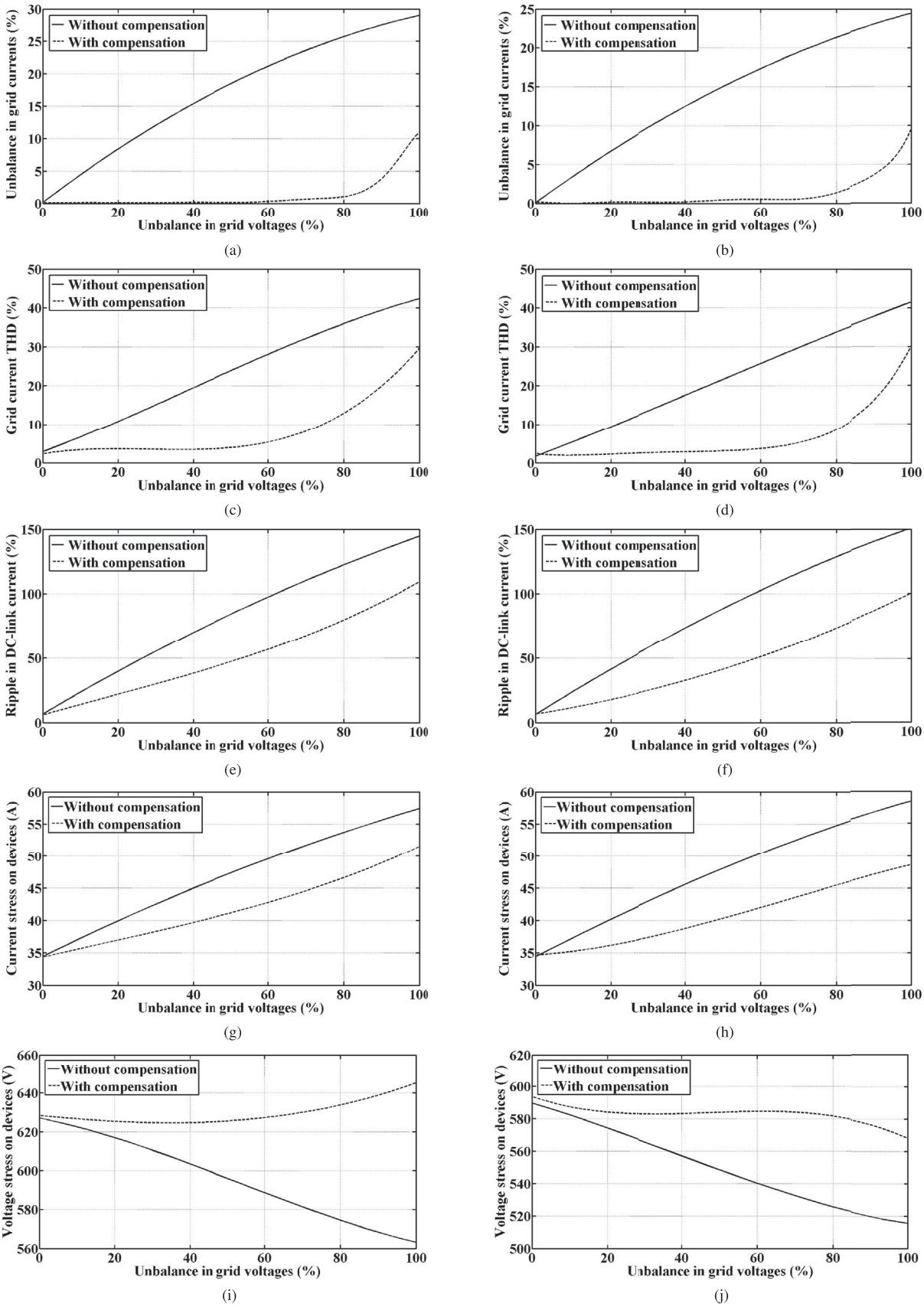

Fig. 15. Simulation results: Improvements with the proposed control scheme: three-phase grid current unbalance for (a) inverter mode and (b) rectifier mode; grid current THD for (c) inverter mode and (d) rectifier mode; peak-to-peak ripple in dc-link current for (e) inverter mode and (f) rectifier mode; current stress on devices for (g) inverter mode and (h) rectifier mode; voltage stress on devices for (i) inverter mode and (j) rectifier mode.

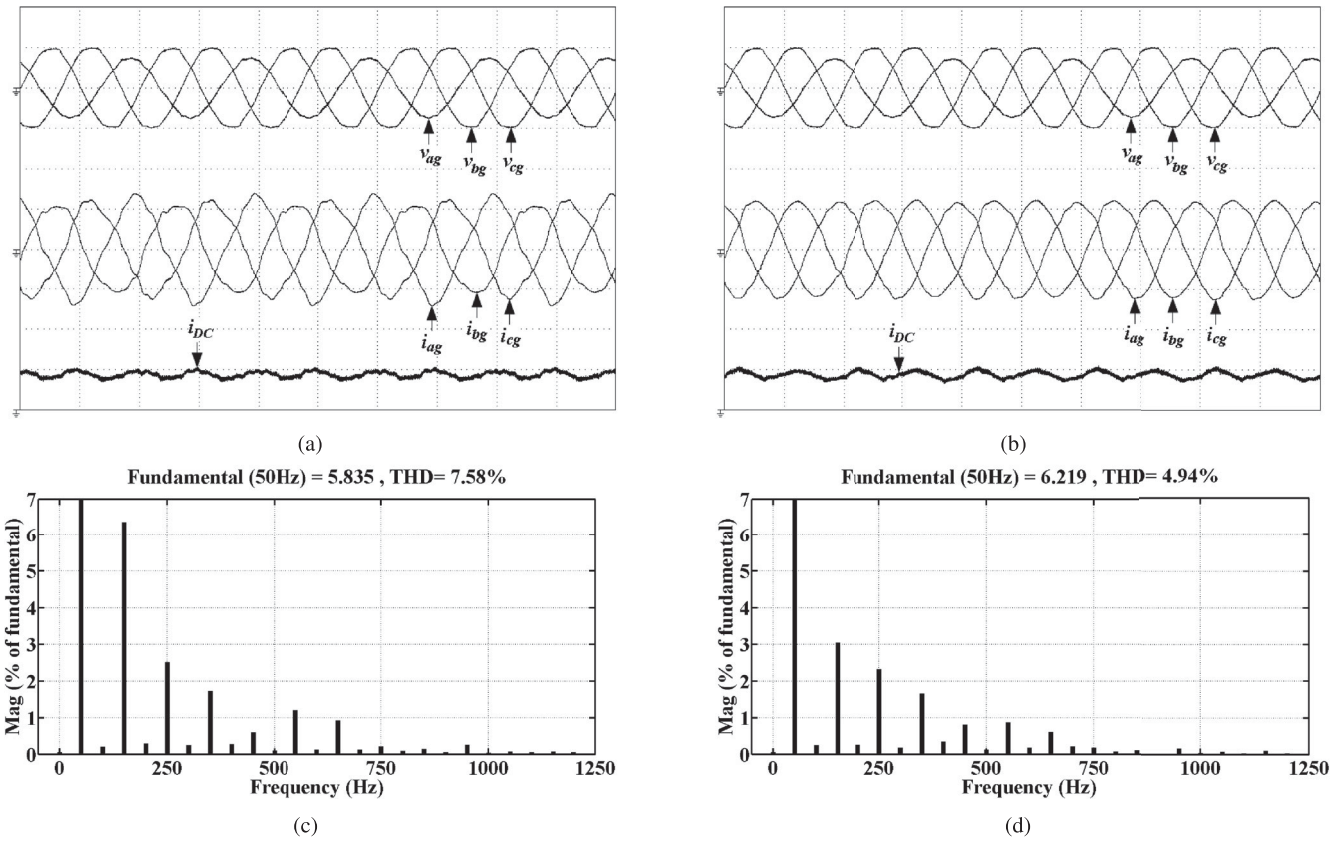

Fig. 16. Experimental results: Inverter mode of operation: (a) Without compensation. (b) With proposed control scheme. Grid voltages $v_{\rm ag}$, $v_{\rm bg}$, and $v_{\rm cg}$ (100 V/div); grid currents $i_{\rm ag}$, $i_{\rm bg}$, and $i_{\rm cg}$ (5 A/div); dc-link current $i_{\rm DC}$ (10 A/div); time scale: 10 ms/div. (c) Harmonic spectrum of $i_{\rm ag}$ without compensation. (d) Harmonic spectrum of $i_{\rm ag}$ with the proposed control scheme.

Rearranging the terms gives

$$V_{\rm BUS}+\widehat{v}_{\rm BUS}(t)-L_{\rm DC}\frac{dI_{\rm DC}}{dt}-L_{\rm DC}\frac{d\widehat{i}_{\rm DC}(t)}{dt} -\frac{3}{2}[V_d+\widehat{v}_d(t)]\frac{I_d}{I_{\rm DC}}\left[\frac{1+\frac{\widehat{i}_d(t)}{I_d}}{1+\frac{\widehat{i}_{\rm DC}(t)}{I_{\rm DC}}}\right] -\frac{3}{2}[V_q+\widehat{v}_q(t)]\frac{I_q}{I_{\rm DC}}\left[\frac{1+\frac{\widehat{i}_q(t)}{I_q}}{1+\frac{\widehat{i}_{\rm DC}(t)}{I_{\rm DC}}}\right]=0. \quad (30)$$

Using power series theorem, and neglecting higher order terms

$$\left[\frac{1}{1+\frac{\widehat{i}_{\rm DC}(t)}{I_{\rm DC}}}\right]=\left[1-\frac{\widehat{i}_{\rm DC}(t)}{I_{\rm DC}}\right]. \quad (31)$$

Using (31) in (30) gives

$$V_{\rm BUS}+\widehat{v}_{\rm BUS}(t)-L_{\rm DC}\frac{dI_{\rm DC}}{dt}-L_{\rm DC}\frac{d\widehat{i}_{\rm DC}(t)}{dt} -\frac{3}{2}[V_d+\widehat{v}_d(t)]\frac{I_d}{I_{\rm DC}}\left[1+\frac{\widehat{i}_d(t)}{I_d}\right]\left[1-\frac{\widehat{i}_{\rm DC}(t)}{I_{\rm DC}}\right] -\frac{3}{2}[V_q+\widehat{v}_q(t)]\frac{I_q}{I_{\rm DC}}\left[1+\frac{\widehat{i}_q(t)}{I_q}\right]\left[1-\frac{\widehat{i}_{\rm DC}(t)}{I_{\rm DC}}\right]=0. \quad (32)$$

After simplification, dc (steady state) terms add up to zero. Neglecting the product terms of two ac terms, a linearized small-signal equation is obtained as

$$\widehat{v}_{\rm BUS}(t)-L_{\rm DC}\frac{d\widehat{i}_{\rm DC}(t)}{dt} +\frac{3}{2}\frac{V_dI_d}{I_{\rm DC}^2}\widehat{i}_{\rm DC}(t)-\frac{3}{2}\frac{V_d}{I_{\rm DC}}\widehat{i}_d(t)-\frac{3}{2}\frac{I_d}{I_{\rm DC}}\widehat{v}_d(t) +\frac{3}{2}\frac{V_qI_q}{I_{\rm DC}^2}\widehat{i}_{\rm DC}(t)-\frac{3}{2}\frac{V_q}{I_{\rm DC}}\widehat{i}_q(t)-\frac{3}{2}\frac{I_q}{I_{\rm DC}}\widehat{v}_q(t)=0. \quad (33)$$

The ac equation is

$$\widehat{v}_{\rm BUS}(s)-sL_{\rm DC}\widehat{i}_{\rm DC}(s) +\frac{3}{2}\frac{V_dI_d}{I_{\rm DC}^2}\widehat{i}_{\rm DC}(s)-\frac{3}{2}\frac{V_d}{I_{\rm DC}}\widehat{i}_d(s)-\frac{3}{2}\frac{I_d}{I_{\rm DC}}\widehat{v}_d(s) +\frac{3}{2}\frac{V_qI_q}{I_{\rm DC}^2}\widehat{i}_{\rm DC}(s)-\frac{3}{2}\frac{V_q}{I_{\rm DC}}\widehat{i}_q(s)-\frac{3}{2}\frac{I_q}{I_{\rm DC}}\widehat{v}_q(s)=0. \quad (34)$$

The converter transfer function $\frac{\widehat{i}_{\rm DC}(s)}{\widehat{i}_d(s)}$ is obtained using (34) as

$$G_c(s)=\frac{\widehat{i}_{\rm DC}(s)}{\widehat{i}_d(s)}=\frac{\frac{3}{2}\frac{V_d}{I_{\rm DC}}}{\left[-sL_{\rm DC}+\frac{3}{2}\frac{V_dI_d}{I_{\rm DC}^2}+\frac{3}{2}\frac{V_qI_q}{I_{\rm DC}^2}\right]}. \quad (35)$$

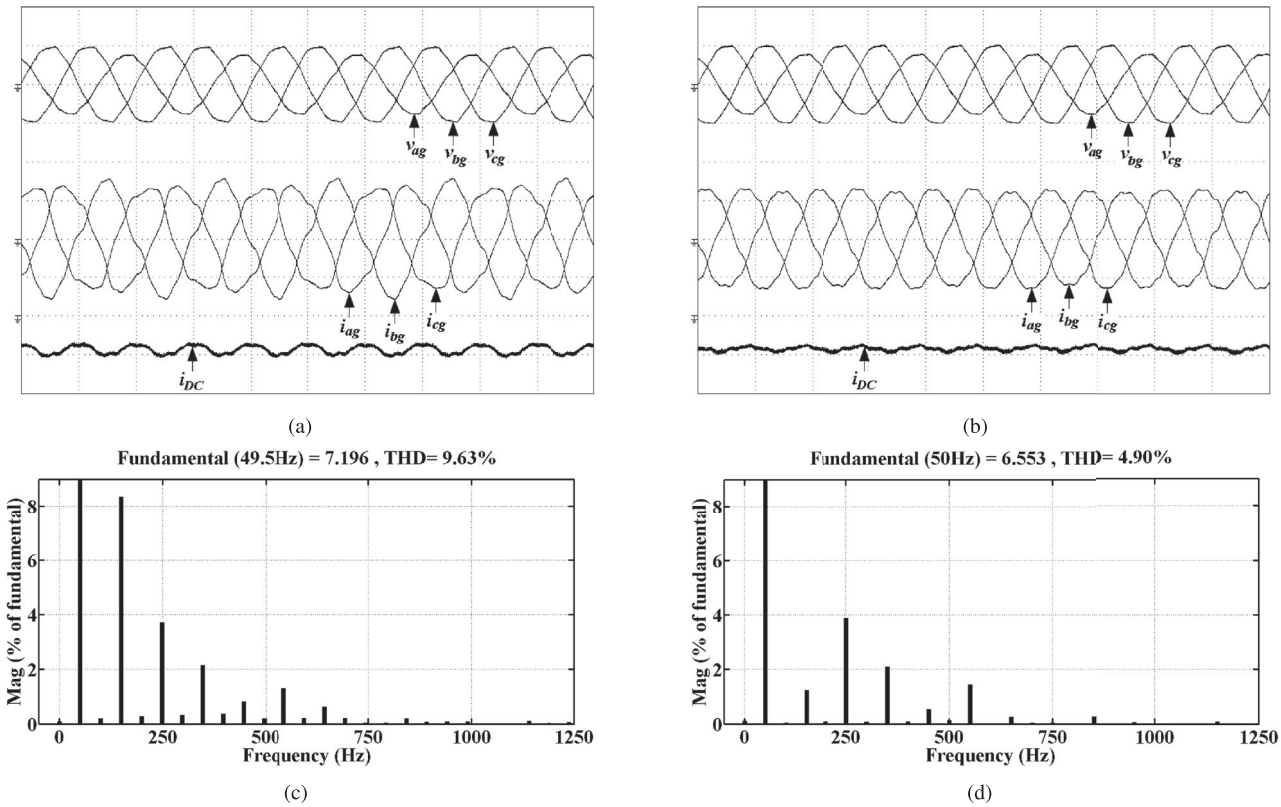

Fig. 17. Experimental results: Rectifier mode of operation: (a) Without compensation. (b) With proposed control scheme. Grid voltages $v_{\rm ag}$, $v_{\rm bg}$, and $v_{\rm cg}$ (100 V/div); grid currents $i_{\rm ag}$, $i_{\rm bg}$, and $i_{\rm cg}$ (5 A/div); dc-link current $i_{\rm DC}$ (10 A/div); time scale: 10 ms/div. (c) Harmonic spectrum of $i_{\rm ag}$ without compensation. (d) Harmonic spectrum of $i_{\rm ag}$ with the proposed control scheme.

The transfer function of the PI regulator is

$$G_{\rm PI}(s) = \frac{K_P(s + \frac{K_I}{K_P})}{s}. \tag{36}$$

The stability of the control block diagram shown in Fig. 5 is analyzed by plotting root loci for the loop transfer function

$$G_c(s) \cdot G_{\rm PI}(s) \tag{37}$$

and using the converter parameters given in Table III. Here, $V_d = 240\sqrt{2} = 339$ V, V_q=0 V, I_q= 0 A. Further, $I_{\rm DC} = 33.33$ A, I_d=19.7 A, $K_P = -1$, and $K_I = -0.1$ for inverter mode of operation. For rectifier mode of operation, $I_{\rm DC} = -33.33$ A, $I_d = -19.7$ A, K_P= 1, and $K_I = 0.1$. The root loci for these two modes are shown in Fig. 6.

Appendix B
Stability Analysis of the Closed-Loop Controller Using the Modified Control Scheme

Stability of the closed-loop controller shown in Fig. 7 is analyzed by plotting root loci of the loop transfer function

$$G_c(s) \cdot G_{\rm PI}(s) \cdot G_f(s) \tag{38}$$

where $G_c(s)$ and $G_{\rm PI}(s)$ are given by (35) and (36), respectively, and $G_f(s)$ is the notch filter transfer function

$$G_f(s) = \frac{s^2 + \omega^2}{s^2 + 2\zeta\omega s + \omega^2}. \tag{39}$$

Here, the cutoff frequency $\omega = 628.3$ rad/s, and the damping coefficient $\zeta = 0.707$. The root loci for inverter and rectifier modes are shown in Fig. 8.

Appendix C
Stability Analysis of the Closed-Loop Controller Using the Proposed Control Scheme

Equation (27) can also be written as

$$\langle v_{\rm DC}(t)\rangle_{Ts} = \frac{3}{2}\langle v_d(t)\rangle_{Ts}\langle m_d(t)\rangle_{Ts} + \frac{3}{2}\langle v_q(t)\rangle_{Ts}\langle m_q(t)\rangle_{Ts}. \tag{40}$$

Using (40) in (25) gives

$$\langle v_{\rm BUS}(t)\rangle_{Ts} - L_{\rm DC}\frac{d\langle i_{\rm DC}(t)\rangle_{Ts}}{dt} - \frac{3}{2}\langle v_d(t)\rangle_{Ts}\langle m_d(t)\rangle_{Ts} - \frac{3}{2}\langle v_q(t)\rangle_{Ts}\langle m_q(t)\rangle_{Ts} = 0. \tag{41}$$

After applying small perturbation, (41) becomes

$$V_{\rm BUS} + \widehat{v}_{\rm BUS}(t) - L_{\rm DC}\frac{dI_{\rm DC}}{dt} - L_{\rm DC}\frac{d\widehat{i}_{\rm DC}(t)}{dt} - \frac{3}{2}\left[V_d + \widehat{v}_d(t)\right]\left[M_d + \widehat{m}_d(t)\right] - \frac{3}{2}\left[V_q + \widehat{v}_q(t)\right]\left[M_q + \widehat{m}_q(t)\right] = 0. \tag{42}$$

After simplification, dc (steady state) terms add up to zero. Neglecting the product terms of two ac terms, a linearized small-signal equation is obtained as

$$\widehat{v}_{\rm BUS}(t) - L_{\rm DC}\frac{d\widehat{i}_{\rm DC}(t)}{dt} - \frac{3}{2}V_d\widehat{m}_d(t) - \frac{3}{2}\widehat{v}_d(t)M_d - \frac{3}{2}V_q\widehat{m}_q(t) - \frac{3}{2}\widehat{v}_q(t)M_q = 0. \quad (43)$$

The ac equation is

$$\widehat{v}_{\rm BUS}(s) - sL_{\rm DC}\widehat{i}_{\rm DC}(s) - \frac{3}{2}V_d\widehat{m}_d(s) - \frac{3}{2}\widehat{v}_d(s)M_d - \frac{3}{2}V_q\widehat{m}_q(s) - \frac{3}{2}\widehat{v}_q(s)M_q = 0. \quad (44)$$

The converter transfer function $\frac{\widehat{i}_{\rm DC}(s)}{\widehat{m}_d(s)}$ is obtained using (44) as

$$G_c(s) = \frac{\widehat{i}_{\rm DC}(s)}{\widehat{m}_d(s)} = \frac{-\frac{3}{2}V_d}{sL_{\rm DC}}. \quad (45)$$

Stability of the closed-loop controller is analyzed by plotting root locus of the loop transfer function

$$G_c(s)\cdot G_{\rm PI}(s)\cdot G_f(s) \quad (46)$$

where $G_{\rm PI}(s)$ and $G_f(s)$ are given by (36) and (39), respectively, and $V_d = 339$ V, K_P=−1, K_I=−0.1, $\omega = 628.3$ rad/s, and $\zeta = 0.707$.

It should be noted that the converter transfer function represented by (45) depends on d-axis voltage only, unlike (35). Therefore, it has identical root loci for inverter and rectifier modes of operation. The root locus is shown in Fig. 10.

Appendix D
Mathematical Expression for the Modulation Index m

After expanding the higher power terms in (13)

$$\begin{aligned} m = \; & I^*\Bigg\{\frac{1}{I_{\rm DC}} - \frac{[I_{\rm dcc}\cos(2\omega t) + I_{\rm dcs}\sin(2\omega t)]}{I_{\rm DC}^2} \\ & + \frac{\begin{bmatrix} I_{\rm dcc}^2\cos^2(2\omega t) + I_{\rm dcs}^2\sin^2(2\omega t) \\ +2\; I_{\rm dcc}I_{\rm dcs}\cos(2\omega t)\sin(2\omega t)\end{bmatrix}}{I_{\rm DC}^3} \\ & - \frac{\begin{bmatrix} I_{\rm dcc}^3\cos^3(2\omega t) + I_{\rm dcs}^3\sin^3(2\omega t) \\ +3I_{\rm dcc}^2\; I_{\rm dcs}\cos^2(2\omega t)\sin(2\omega t) \\ +3I_{\rm dcc}I_{\rm dcs}^2\cos(2\omega t)\sin^2(2\omega t)\end{bmatrix}}{I_{\rm DC}^4} + \cdots\Bigg\}. \end{aligned} \quad (47)$$

Simplification using the trigonometric identities gives

$$\begin{aligned} m = \; & I^*\Bigg\{\frac{1}{I_{\rm DC}} - \frac{[I_{\rm dcc}\cos(2\omega t) + I_{\rm dcs}\sin(2\omega t)]}{I_{\rm DC}^2} \\ & + \frac{\begin{bmatrix} \frac{I_{\rm dcc}^2}{2} + \frac{I_{\rm dcc}^2}{2}\cos(4\omega t) + \frac{I_{\rm dcs}^2}{2} \\ -\frac{I_{\rm dcs}^2}{2}\cos(4\omega t) + I_{\rm dcc}I_{\rm dcs}\sin(4\omega t)\end{bmatrix}}{I_{\rm DC}^3} \\ & - \frac{\begin{bmatrix} \frac{3I_{\rm dcc}^3}{4}\cos(2\omega t) + \frac{3I_{\rm dcc}^2\; I_{\rm dcs}}{4}\sin(2\omega t) \\ +\frac{I_{\rm dcc}^3}{4}\cos(6\omega t) + \frac{3I_{\rm dcc}^2\; I_{\rm dcs}}{4}\sin(6\omega t) \\ +\frac{3I_{\rm dcc}I_{\rm dcs}^2}{4}\cos(2\omega t) + \frac{3I_{\rm dcs}^3}{4}\sin(2\omega t) \\ -\frac{3I_{\rm dcc}I_{\rm dcs}^2}{4}\cos(6\omega t) - \frac{I_{\rm dcs}^3}{4}\sin(6\omega t)\end{bmatrix}}{I_{\rm DC}^4} + \cdots\Bigg\}. \end{aligned} \quad (48)$$

After rearranging the terms, m can be expressed as in (14).

Appendix E
Necessary Condition for M_c and M_s to Eliminate the Negative-Sequence Components From Grid Currents

After simplification, and using the trigonometric identities, (16) can be written as

$$\begin{aligned} \bar{i}_g = \; & [MI_{\rm DC} + MI_{\rm dcc}\cos(2\omega t) + MI_{\rm dcs}\sin(2\omega t) \\ & + M_cI_{\rm DC}\cos(2\omega t) + \frac{M_cI_{\rm dcc}}{2} + \frac{M_cI_{\rm dcc}}{2}\cos(4\omega t) \\ & + \frac{M_cI_{\rm dcs}}{2}\sin(4\omega t) + M_sI_{\rm DC}\sin(2\omega t) \\ & + \frac{M_sI_{\rm dcc}}{2}\sin(4\omega t) + \frac{M_sI_{\rm dcs}}{2} - \frac{M_sI_{\rm dcs}}{2}\cos(4\omega t)] \\ & \times [\cos(\omega t+\phi) + j\sin(\omega t+\phi)]. \end{aligned} \quad (49)$$

After simplifying and applying the trigonometric identities

$$\begin{aligned} \bar{i}_g = \; & MI_{\rm DC}\cos(\omega t+\phi) + jMI_{\rm DC}\sin(\omega t+\phi) \\ & + \frac{MI_{\rm dcc}}{2}\cos(\omega t-\phi) + \frac{MI_{\rm dcc}}{2}\cos(3\omega t+\phi) \\ & + j\frac{MI_{\rm dcc}}{2}\sin(3\omega t+\phi) - j\frac{MI_{\rm dcc}}{2}\sin(\omega t-\phi) \\ & + \frac{MI_{\rm dcs}}{2}\sin(3\omega t+\phi) + \frac{MI_{\rm dcs}}{2}\sin(\omega t-\phi) \\ & + j\frac{MI_{\rm dcs}}{2}\cos(\omega t-\phi) - j\frac{MI_{\rm dcs}}{2}\cos(3\omega t+\phi) \\ & + \frac{M_cI_{\rm DC}}{2}\cos(\omega t-\phi) + \frac{M_cI_{\rm DC}}{2}\cos(3\omega t+\phi) \\ & + j\frac{M_cI_{\rm DC}}{2}\sin(3\omega t+\phi) - j\frac{M_cI_{\rm DC}}{2}\sin(\omega t-\phi) \\ & + \frac{M_cI_{\rm dcc}}{2}\cos(\omega t+\phi) + j\frac{M_cI_{\rm dcc}}{2}\sin(\omega t+\phi) \\ & + \frac{M_cI_{\rm dcc}}{4}\cos(3\omega t-\phi) + \frac{M_cI_{\rm dcc}}{4}\cos(5\omega t+\phi) \\ & + j\frac{M_cI_{\rm dcc}}{4}\sin(5\omega t+\phi) - j\frac{M_cI_{\rm dcc}}{4}\sin(3\omega t-\phi) \\ & + \frac{M_cI_{\rm dcs}}{4}\sin(5\omega t+\phi) + \frac{M_cI_{\rm dcs}}{4}\sin(3\omega t-\phi) \\ & + j\frac{M_cI_{\rm dcs}}{4}\cos(3\omega t-\phi) - j\frac{M_cI_{\rm dcs}}{4}\cos(5\omega t+\phi) \\ & + \frac{M_sI_{\rm DC}}{2}\sin(3\omega t+\phi) + \frac{M_sI_{\rm DC}}{2}\sin(\omega t-\phi) \end{aligned}$$

$$
\begin{aligned}
&+j\frac{M_s I_{\rm DC}}{2}\cos(\omega t-\phi)-j\frac{M_s I_{\rm DC}}{2}\cos(3\omega t+\phi)\\
&+\frac{M_s I_{\rm dcc}}{4}\sin(5\omega t+\phi)+\frac{M_s I_{\rm dcc}}{4}\sin(3\omega t-\phi)\\
&+j\frac{M_s I_{\rm dcc}}{4}\cos(3\omega t-\phi)-j\frac{M_s I_{\rm dcc}}{4}\cos(5\omega t+\phi)\\
&+\frac{M_s I_{\rm dcs}}{2}\cos(\omega t+\phi)+j\frac{M_s I_{\rm dcs}}{2}\sin(\omega t+\phi)\\
&-\frac{M_s I_{\rm dcs}}{4}\cos(3\omega t-\phi)-\frac{M_s I_{\rm dcs}}{4}\cos(5\omega t+\phi)\\
&-j\frac{M_s I_{\rm dcs}}{4}\sin(5\omega t+\phi)+j\frac{M_s I_{\rm dcs}}{4}\sin(3\omega t-\phi). \quad (50)
\end{aligned}
$$

After rearranging the terms, the expression for the grid current space vector can be written as (17).

Appendix F
Stability of the Negative-Sequence Currents (i_d^- and i_q^-) Regulating Loops

Under unbalanced grid voltage condition, the power balance equation between converter dc and ac sides can be written using dq-axis positive- and negative-sequence components of the grid voltage and grid current as [16], [22]–[25]

$$
\begin{aligned}
v_{\rm DC}i_{\rm DC} = {}& \frac{3}{2}[v_d^+ i_d^+ + v_q^+ i_q^+ + v_d^- i_d^- + v_q^- i_q^-]\\
&+\frac{3}{2}[v_d^+ i_d^- + v_q^+ i_q^- + v_d^- i_d^+ + v_q^- i_q^+]\cos(2\omega t)\\
&+\frac{3}{2}[v_d^+ i_q^- - v_q^+ i_d^- + v_q^- i_d^+ - v_d^- i_q^+]\sin(2\omega t). \quad (51)
\end{aligned}
$$

This is a periodically time-varying system. Hence, the averaged equation can be written by time-averaging over a fundamental period as [51], [52]

$$
\begin{aligned}
\langle v_{\rm DC}(t)\rangle_{Tf}\langle i_{\rm DC}(t)\rangle_{Tf} = {}& \frac{3}{2}\langle v_d^+(t)\rangle_{Tf}\langle i_d^+(t)\rangle_{Tf}\\
&+\frac{3}{2}\langle v_q^+(t)\rangle_{Tf}\langle i_q^+(t)\rangle_{Tf}\\
&+\frac{3}{2}\langle v_d^-(t)\rangle_{Tf}\langle i_d^-(t)\rangle_{Tf}\\
&+\frac{3}{2}\langle v_q^-(t)\rangle_{Tf}\langle i_q^-(t)\rangle_{Tf}. \quad (52)
\end{aligned}
$$

Therefore

$$
\begin{aligned}
\langle v_{\rm DC}(t)\rangle_{Tf} = {}& \frac{3}{2}\langle v_d^+(t)\rangle_{Tf}\langle m_d(t)\rangle_{Tf}\\
&+\frac{3}{2}\langle v_q^+(t)\rangle_{Tf}\langle m_q(t)\rangle_{Tf}\\
&+\frac{3}{2}\langle v_d^-(t)\rangle_{Tf}\langle m_c(t)\rangle_{Tf}\\
&+\frac{3}{2}\langle v_q^-(t)\rangle_{Tf}\langle m_s(t)\rangle_{Tf}. \quad (53)
\end{aligned}
$$

Equation (52) can also be written as

$$
\begin{aligned}
\langle i_{\rm DC}(t)\rangle_{Tf} = {}& \frac{\langle i_d^+(t)\rangle_{Tf}}{\langle m_d(t)\rangle_{Tf}}+\frac{\langle i_q^+(t)\rangle_{Tf}}{\langle m_q(t)\rangle_{Tf}}\\
&+\frac{\langle i_d^-(t)\rangle_{Tf}}{\langle m_c(t)\rangle_{Tf}}+\frac{\langle i_q^-(t)\rangle_{Tf}}{\langle m_s(t)\rangle_{Tf}}. \quad (54)
\end{aligned}
$$

Using (53) and (54) in (25) gives

$$
\begin{aligned}
&\langle v_{\rm BUS}(t)\rangle_{Tf}-L_{\rm DC}\frac{d}{dt}\begin{bmatrix}\frac{\langle i_d^+(t)\rangle_{Tf}}{\langle m_d(t)\rangle_{Tf}}+\frac{\langle i_q^+(t)\rangle_{Tf}}{\langle m_q(t)\rangle_{Tf}}\\ +\frac{\langle i_d^-(t)\rangle_{Tf}}{\langle m_c(t)\rangle_{Tf}}+\frac{\langle i_q^-(t)\rangle_{Tf}}{\langle m_s(t)\rangle_{Tf}}\end{bmatrix}\\
&\qquad -\frac{3}{2}\begin{bmatrix}\langle v_d^+(t)\rangle_{Tf}\langle m_d(t)\rangle_{Tf}\\ +\langle v_q^+(t)\rangle_{Tf}\langle m_q(t)\rangle_{Tf}\\ +\langle v_d^-(t)\rangle_{Tf}\langle m_c(t)\rangle_{Tf}\\ +\langle v_q^-(t)\rangle_{Tf}\langle m_s(t)\rangle_{Tf}\end{bmatrix}=0. \quad (55)
\end{aligned}
$$

After applying small perturbation, (55) becomes

$$
\begin{aligned}
&V_{\rm BUS}+\widehat{v}_{\rm BUS}(t)\\
&\quad -L_{\rm DC}\frac{d}{dt}\begin{bmatrix}\frac{I_d^+ +\widehat{i}_d^+(t)}{M_d+\widehat{m}_d(t)}+\frac{I_q^+ +\widehat{i}_q^+(t)}{M_q+\widehat{m}_q(t)}\\ +\frac{I_d^- +\widehat{i}_d^-(t)}{M_c+\widehat{m}_c(t)}+\frac{I_q^- +\widehat{i}_q^-(t)}{M_s+\widehat{m}_s(t)}\end{bmatrix}\\
&\quad -\frac{3}{2}\begin{bmatrix}[V_d^+ +\widehat{v}_d^+(t)][M_d+\widehat{m}_d(t)]\\ +[V_q^+ +\widehat{v}_q^+(t)][M_q+\widehat{m}_q(t)]\\ +[V_d^- +\widehat{v}_d^-(t)][M_c+\widehat{m}_c(t)]\\ +[V_q^- +\widehat{v}_q^-(t)][M_s+\widehat{m}_s(t)]\end{bmatrix}=0. \quad (56)
\end{aligned}
$$

Rearranging the terms, and using the power series theorem, (56) can be written as

$$
\begin{aligned}
&V_{\rm BUS}+\widehat{v}_{\rm BUS}(t)\\
&\quad -L_{\rm DC}\frac{d}{dt}\begin{bmatrix}\frac{I_d^+}{M_d}\left[1+\frac{\widehat{i}_d^+(t)}{I_d^+}\right]\left[1-\frac{\widehat{m}_d(t)}{M_d}\right]\\ +\frac{I_q^+}{M_q}\left[1+\frac{\widehat{i}_q^+(t)}{I_q^+}\right]\left[1-\frac{\widehat{m}_q(t)}{M_q}\right]\\ +\frac{I_d^-}{M_c}\left[1+\frac{\widehat{i}_d^-(t)}{I_d^-}\right]\left[1-\frac{\widehat{m}_c(t)}{M_c}\right]\\ +\frac{I_q^-}{M_s}\left[1+\frac{\widehat{i}_q^-(t)}{I_q^-}\right]\left[1-\frac{\widehat{m}_s(t)}{M_s}\right]\end{bmatrix}\\
&\quad -\frac{3}{2}\begin{bmatrix}[V_d^+ +\widehat{v}_d^+(t)][M_d+\widehat{m}_d(t)]\\ +[V_q^+ +\widehat{v}_q^+(t)][M_q+\widehat{m}_q(t)]\\ +[V_d^- +\widehat{v}_d^-(t)][M_c+\widehat{m}_c(t)]\\ +[V_q^- +\widehat{v}_q^-(t)][M_s+\widehat{m}_s(t)]\end{bmatrix}=0. \quad (57)
\end{aligned}
$$

After simplification, dc (steady state) terms add up to zero. Neglecting the product terms of two ac terms, a linearized small-signal equation is obtained as

$$
\widehat{v}_{\rm BUS}(t)+L_{\rm DC}\begin{bmatrix}\frac{I_d^+}{M_d^2}\frac{d\widehat{m}_d(t)}{dt}-\frac{1}{M_d}\frac{d\widehat{i}_d^+(t)}{dt}\\ +\frac{I_q^+}{M_q^2}\frac{d\widehat{m}_q(t)}{dt}-\frac{1}{M_q}\frac{d\widehat{i}_q^+(t)}{dt}\\ +\frac{I_d^-}{M_c^2}\frac{d\widehat{m}_c(t)}{dt}-\frac{1}{M_c}\frac{d\widehat{i}_d^-(t)}{dt}\\ +\frac{I_q^-}{M_s^2}\frac{d\widehat{m}_s(t)}{dt}-\frac{1}{M_s}\frac{d\widehat{i}_q^-(t)}{dt}\end{bmatrix}
$$

$$-\frac{3}{2}\begin{bmatrix} V_d^+\widehat{m}_d(t)+M_d\widehat{v}_d^+(t) \\ +V_q^+\widehat{m}_q(t)+M_q\widehat{v}_q^+(t) \\ +V_d^-\widehat{m}_c(t)+M_c\widehat{v}_d^-(t) \\ +V_q^-\widehat{m}_s(t)+M_s\widehat{v}_q^-(t)\end{bmatrix}=0. \tag{58}$$

The ac equation is

$$\widehat{v}_{\rm BUS}(s)+sL_{\rm DC}\begin{bmatrix} \frac{I_d^+}{M_d^2}\widehat{m}_d(s)-\frac{1}{M_d}\widehat{i}_d^+(s) \\ +\frac{I_q^+}{M_q^2}\widehat{m}_q(s)-\frac{1}{M_q}\widehat{i}_q^+(s) \\ +\frac{I_d^-}{M_c^2}\widehat{m}_c(s)-\frac{1}{M_c}\widehat{i}_d^-(s) \\ +\frac{I_q^-}{M_s^2}\widehat{m}_s(s)-\frac{1}{M_s}\widehat{i}_q^-(s)\end{bmatrix}$$

$$-\frac{3}{2}\begin{bmatrix} V_d^+\widehat{m}_d(s)+M_d\widehat{v}_d^+(s) \\ +V_q^+\widehat{m}_q(s)+M_q\widehat{v}_q^+(s) \\ +V_d^-\widehat{m}_c(s)+M_c\widehat{v}_d^-(s) \\ +V_q^-\widehat{m}_s(s)+M_s\widehat{v}_q^-(s)\end{bmatrix}=0. \tag{59}$$

The converter transfer function $\frac{\widehat{i}_d^-(s)}{\widehat{m}_c(s)}$ is obtained using (59) as

$$G_{cd}(s)=\frac{\widehat{i}_d^-(s)}{\widehat{m}_c(s)}=\frac{s2L_{\rm DC}I_d^- - 3V_d^-M_c^2}{s2L_{\rm DC}M_c} \tag{60}$$

whereas the converter transfer function $\frac{\widehat{i}_q^-(s)}{\widehat{m}_s(s)}$ is obtained using (59) as

$$G_{cq}(s)=\frac{\widehat{i}_q^-(s)}{\widehat{m}_s(s)}=\frac{s2L_{\rm DC}I_q^- - 3V_q^-M_s^2}{s2L_{\rm DC}M_s}. \tag{61}$$

The fundamental frequency positive-sequence, fundamental frequency negative-sequence, third-harmonic positive-sequence, third-harmonic negative-sequence, and fifth-harmonic positive-sequence current components present in the grid currents will appear as 100 Hz, DC, 200 Hz, 100 Hz, and 300 Hz in a negatively rotating synchronous reference frame, respectively. These pulsating current components are filtered using notch filters $G_{f1}(s)$, $G_{f2}(s)$, and $G_{f3}(s)$, which has a transfer function similar to (39). The stability of the negative-sequence current regulating loops is analyzed by plotting root loci for the loop transfer functions

$$G_{cd}(s)\cdot G_{f1}(s)\cdot G_{f2}(s)\cdot G_{f3}(s)\cdot G_{\rm PI}(s) \tag{62}$$

and

$$G_{cq}(s)\cdot G_{f1}(s)\cdot G_{f2}(s)\cdot G_{f3}(s)\cdot G_{\rm PI}(s). \tag{63}$$

Here, $V_d^-=-105$ V, V_q^-=−105 V, I_d^-=I_q^-=0, $M_c=-0.22$, and M_s=0.22. Further, $K_P=-1$ and $K_I=-0.1$ for (62) (i_d^- regulating loop). $K_P=1$ and $K_I=0.1$ for (63) (i_q^- regulating loop). The root locus for these to control loops is shown in Fig. 11.

REFERENCES

[1] A. Lahyani, P. Venet, G. Grellet, and P. J. Viverge, "Failure prediction of electrolytic capacitors during operation of a switchmode power supply," *IEEE Trans. Power Electron.*, vol. 13, no. 6, pp. 1199–1207, Nov. 1998.

[2] J. M. Galvez and M. Ordonez, "Swinging bus operation of inverters for fuel cell applications with small DC-link capacitance," *IEEE Trans. Power Electron.*, vol. 30, no. 2, pp. 1064–1075, Feb. 2015.

[3] W. Huai, M. Ke, and F. Blaabjerg, "Design for reliability of power electronic systems," in *Proc. IEEE Ind. Electron. Soc. Conf.*, 2012, pp. 33–44.

[4] E. Wolfgang, "Examples for failures in power electronics systems," presented at the ECPE Tut. Rel. Power Electron. Syst., Nuremberg, Germany, Apr. 2007.

[5] W. Huai and F. Blaabjerg, "Reliability of capacitors for DC-Link applications in power electronic converters-an overview," *IEEE Trans. Ind. Appl.*, vol. 50, no. 5, pp. 3569–3578, Sep./Oct. 2014.

[6] D. Winterborne, M. Mingyao, W. Haimeng, V. Pickert, J. Widmer, P. Barrass, and L. Shah, "Capacitors for high temperature DC link applications in automotive traction drives: Current technology and limitations," in *Proc. IEEE Eur. Power Electron. Appl. Conf.*, 2013, pp. 1–7.

[7] A. Sannino, G. Postiglione, and M. H. J. Bollen, "Feasibility of a dc network for commercial facilities," *IEEE Trans. Ind. Appl.*, vol. 39, no. 5, pp. 1499–1507, Sep. 2003.

[8] B. Mirafzal, M. Saghaleini, and A. Kaviani, "An SVPWM-based switching pattern for stand-alone and grid-connected three-phase single-stage boost inverters," *IEEE Trans. Power Electron.*, vol. 26, no. 4, pp. 1102–1111, Apr. 2011.

[9] P. P. Dash and M. Kazerani, "Dynamic modeling and performance analysis of a grid-connected current-source inverter-based photovoltaic system," *IEEE Trans. Sustain. Energy*, vol. 2, no. 4, pp. 443–450, Oct. 2011.

[10] B. Sahan, S. V. Arajo, C. Nding, and P. Zacharias, "Comparative evaluation of three-phase current source inverters for grid interfacing of distributed and renewable energy systems," *IEEE Trans. Power Electron.*, vol. 26, no. 8, pp. 2304–2318, Aug. 2011.

[11] Y. Chen and K. Smedley, "Three-phase boost-type grid-connected inverter," *IEEE Trans. Power Electron.*, vol. 23, no. 5, pp. 2301–2309, Sep. 2008.

[12] J. F. Zhao, J. G. Jiang, and X. W. Yang, "AC-DC-DC isolated converter with bidirectional power flow capability," *Power Electron., IET*, vol. 3, no. 4, pp. 472–479, Jul. 2010.

[13] T. C. Green, M. H. Taha, N. A. Rahim, and B. W. Williams, "Three-phase step-down reversible AC-DC power converter," *IEEE Trans. Power Electron.*, vol. 12, no. 2, pp. 319–324, Mar. 1997.

[14] V. Vekhande and B. G. Fernandes, "Bidirectional current-fed converter for integration of DC micro-grid with AC grid," in *Proc. Annu. IEEE India Conf.*, 2011, pp. 1–5.

[15] P. N. Enjeti and S. A. Choudhury, "A new control strategy to improve the performance of a PWM AC to DC converter under unbalanced operating conditions," *IEEE Trans. Power Electron.*, vol. 8, no. 4, pp. 493–500, Oct. 1993.

[16] Y. Suh, Y. Go, and D. Rho, "A comparative study on control algorithm for active front-end rectifier of large motor drives under unbalanced input," *IEEE Trans. Ind. Appl.*, vol. 47, no. 3, pp. 1419–1431, Jun. 2011.

[17] A. Yazdani and R. Iravani, "A unified dynamic model and control for the voltage-sourced converter under unbalanced grid conditions," *IEEE Trans. Power Del.*, vol. 21, no. 3, pp. 1620–1629, Jul. 2006.

[18] G. Xiaoqiang, L. Wenzhao, Z. Xue, S. Xiaofeng, L. Zhigang, and J. M. Guerrero, "Flexible control strategy for grid-connected inverter under unbalanced grid faults without PLL," *IEEE Trans. Power Electron.*, vol. 30, no. 4, pp. 1773–1778, Apr. 2015.

[19] L. Yiqi, L. Ningning, F. Yu, W. Jianze, and J. Yanchao, "Stationary-frame-based generalized control diagram for PWM AC-DC front-end converters with unbalanced grid voltage in renewable energy systems," in *Proc. Appl. Power Electron. Conf.*, 2015, pp. 678–683.

[20] J. A. Suul, A. Luna, P. Rodriguez, and T. Undeland, "Virtual-flux-based voltage-sensor-less power control for unbalanced grid conditions," *IEEE Trans. Power Electron.*, vol. 27, no. 9, pp. 4071–4087, Sep. 2012.

[21] Z. Yongchang and Q. Changqi, "Direct power control of a pulse width modulation rectifier using space vector modulation under unbalanced grid voltages," *IEEE Trans. Power Electron.*, vol. 30, no. 10, pp. 5892–5901, Oct. 2015.

[22] Z. Yongchang and Q. Changqi, "Table-based direct power control for three-phase AC/DC converters under unbalanced grid voltages," *IEEE Trans. Power Electron.*, vol. 30, no. 12, pp. 7090–7099, Dec. 2015.

[23] H. Nian, P. Cheng, and Z. Q. Zhu, "Coordinated direct power control of DFIG system without phase locked loop under unbalanced grid voltage conditions," *IEEE Trans. Power Electron.*, vol. 31, no. 4, pp. 2905–2918, Apr. 2016.

[24] K. Ma, W. Chen, M. Liserre, and F. Blaabjerg, "Power controllability of a three-phase converter with an unbalanced AC source," *IEEE Trans. Power Electron.*, vol. 30, no. 3, pp. 1591–1604, Mar. 2015.
[25] M. Zhu, L. Hang, G. Li, and X. Jiang, "Protected control method for power conversion interface under unbalanced operating conditions in AC/DC hybrid distributed grid," *IEEE Trans. Energy Convers.*, vol. PP, no. 99, pp. 1–12.
[26] V. Vekhande, B. B. Pimple, and B. G. Fernandes, "Modulation of indirect matrix converter under unbalanced source voltage condition," in *Proc. IEEE Energy Convers. Congr. Expo.*, 2011, pp. 225–229.
[27] J. Dai, D. Xu, B. Wu, and N. Zargari, "Unified dc-link current control for low-voltage ride-through in current-source-converter-based wind energy conversion systems," *IEEE Trans. Power Electron.*, vol. 26, no. 1, pp. 288–297, Jan. 2011.
[28] M. Tsili and S. Papathanassiou, "A review of grid code technical requirements for wind farms," *IET Renew. Power Generat., IET*, vol. 3, no. 3, pp. 308–332, Sep. 2009.
[29] M. Popat, W. Bin, and N. R. Zargari, "Fault ride-through capability of cascaded current-source converter-based offshore wind farm," *IEEE Trans. Sustain. Energy*, vol. 4, no. 2, pp. 314–323, Apr. 2013.
[30] J. Miret, M. Castilla, A. Camacho, L. G. Vicuna, and J. Matas, "Control scheme for photovoltaic three-phase inverters to minimize peak currents during unbalanced grid-voltage sags," *IEEE Trans. Power Electron.*, vol. 27, no. 10, pp. 4262–4271, Oct. 2012.
[31] F. A. Magueed and J. Svensson, "Control of VSC connected to the grid through LCL filter to achieve balanced currents," in *Proc. IEEE Ind. Appl. Conf.*, 2005, pp. 572–578.
[32] Z. Wang, S. Fan, Z. Zou, Y. Huang, and M. Cheng, "Control strategies of current-source inverters for distributed generation under unbalanced grid conditions," in *Proc. IEEE Energy Convers. Congr. Expo.*, 2012, pp. 4671–4675.
[33] A. Moghadasi and A. Islam, "Enhancing LVRT capability of FSIG wind turbine using current source UPQC based on resistive SFCL," in *Proc. IEEE Trans. Distrib. Conf. Expo.*, 2014, pp. 1–5.
[34] L. Giuntini, M. Crespan, I. Furlan, and S. Colombi, "Robust control of current source rectifier for UPS applications," in *Proc. IEEE Int. Exhib. Conf. Power Electron. Intell. Motion, Renewable Energy Energy Manage.*, 2014, pp. 1–7.
[35] P. E. Melin, J. R. Espinoza, L. A. Moran, J. R. Rodriguez, V. M. Cardenas, C. R. Baier, and J. A. Munoz, "Analysis, design and control of a unified power-quality conditioner based on a current-source topology," *IEEE Trans. Power Del.*, vol. 27, no. 4, pp. 1727–1736, Oct. 2012.
[36] I. Abdelsalam, G. P. Adam, D. Holliday, and B. W. Williams, "Modified back-to-back current source converter and its application to wind energy conversion systems," *IET Power Electron.*, vol. 8, no. 1, pp. 103–111, Jan. 2015.
[37] C. Photong, C. Klumpner, and P. Wheeler, "A current source inverter with series connected AC capacitors for photovoltaic application with grid fault ride through capability," in *Proc. IEEE Ind. Electron. Soc. Conf.*, 2009, pp. 390–396.
[38] X. Wang, Y. Li, F. Blaabjerg, and P. C. Loh, "Virtual-impedance-based control for voltage-source and current-source converters," *IEEE Trans. Power Electron.*, vol. 30, no. 12, pp. 7019–7037, Dec. 2015.
[39] P. C. Loh and D. G. Holmes, "Analysis of multiloop control strategies for LC/CL/LCL-filtered voltage-source and current source inverters," *IEEE Trans. Ind. Appl.*, vol. 41, no. 2, pp. 644–654, Mar. 2005.
[40] H. C. Tay and M. F. Conlon, "Development of an unbalanced switching scheme for a current source inverter," *IET Generat., Transmiss. Distrib.*, vol. 147, no. 1, pp. 23–30, Jan. 2000.
[41] T. Nussbaumer, M. Baumann, and J. W. Kolar, "Comprehensive design of a three-phase three-switch buck-type PWM rectifier," *IEEE Trans. Power Electron.*, vol. 22, no. 2, pp. 551–562, Mar. 2007.
[42] B. Sahan, A. N. Vergara, N. Henze, A. Engler, and P. Zacharias, "A single-stage PV module integrated converter based on a low-power current-source inverter," *IEEE Trans. Ind. Electron.*, vol. 55, no. 7, pp. 2602–2609, Jul. 2008.
[43] M. Salo and H. Tuusa, "A vector-controlled PWM current-source-inverter-fed induction motor drive with a new stator current control method," *IEEE Trans. Ind. Electron.*, vol. 52, no. 2, pp. 523–531, Apr. 2005.
[44] D. N. Zmood and D. G. Holmes, "Improved voltage regulation for current-source inverters," *IEEE Trans. Ind. Appl.*, vol. 37, no. 4, pp. 1028–1036, Aug. 2001.
[45] M. Salo, "A three-switch current-source PWM rectifier with active filter function," in *Proc. IEEE Power Electron. Spec. Conf.*, 2005, pp. 2230–2236.
[46] J. W. Kolar, F. Schafmeister, S. D. Round, and H. Ertl, "Novel three-phase AC-AC sparse matrix converters," *IEEE Trans. Power Electron.*, vol. 22, no. 5, pp. 1649–1661, Sep. 2007.
[47] J. W. Kolar, T. Friedli, F. Krismer, and S. D. Round, "The essence of three-phase AC/AC converter systems," in *Proc. IEEE Power Electron. Motion Control Conf.*, 2008, pp. 27–42.
[48] M. C. Chandorkar, D. M. Divan, and R. H. Lasseter, "Control techniques for multiple current source GTO converters," *IEEE Trans. Ind. Appl.*, vol. 31, no. 1, pp. 134–140, Jan. 1995.
[49] W. Lixiang, T. A. Lipo, and H. Chan, "Matrix converter topologies with reduced number of switches," in *Proc. IEEE Power Electron. Spec. Conf.*, vol. 1, 2002, pp. 57–63.
[50] P. Pillay and M. Manyage, "Definitions of voltage unbalance," *IEEE Power Eng. Rev.*, vol. 21, no. 5, pp. 49–51, May 2001.
[51] M. E. Moursi, K. Goweily, and E. A. Badran, "Enhanced fault ride through performance of self-excited induction generator-based wind park during unbalanced grid operation," *IET Power Electron.*, vol. 6, no. 8, pp. 1683–1695, Sep. 2013.
[52] H. K. Khalil, "Perturbation theory and averaging," in *Nonlinear Systems*, 2nd ed. Upper Saddle River, NJ, USA: Prentice-Hall, 1996, ch. 8, sec. 8.3, pp. 330–339.

Vishal Vekhande (S'12) received the B.E. degree in electrical engineering from Mumbai University, Mumbai, India, in 2005. He is currently working toward the M.Tech.+Ph.D. Dual degree at the Indian Institute of Technology Bombay, Mumbai.

From 2005 to 2007, he was an Executive Engineer with Siemens Ltd., India, as an Executive Engineer. His research interests include power electronic converter topologies for integration of renewable energy sources with ac and dc grids.

Kanakesh V. K. received the M.Tech. degree in electrical engineering from the Indian Institute of Technology Bombay, Mumbai, India, in 2014.

In 2014, he joined the National University of Singapore, where he is currently a Research Engineer and is involved in the development of bidirectional cascaded dc–ac converter for UPS application. His research interests include power electronic interfaces for utility system and high-frequency-link power conversion.

B. G. Fernandes (M'06) received the B.Tech. degree from Mysore University, Mysore, India, in 1984, the M.Tech. degree from the Indian Institute of Technology Kharagpur, India, in 1989, and the Ph.D. degree from the Indian Institute of Technology Bombay, Mumbai, India, in 1993.

He then joined the Department of Electrical Engineering, Indian Institute of Technology, Kanpur, India, as an Assistant Professor. In 1997, he joined Department of Electrical Engineering, Indian Institute of Technology Bombay, where he is currently a Professor. His current research interests include high-performance ac drives, motors for electric vehicles, and power electronic interfaces for nonconventional energy sources.